

# Learning Optimal Forms of Constitutive Relations Characterizing Ion Intercalation from Data in Mathematical Models of Lithium-ion Batteries

Lindsey Daniels,<sup>†</sup> Smita Sahu,<sup>‡,§</sup> Kevin J. Sanders,<sup>¶</sup> Gillian R. Goward,<sup>¶</sup> Jamie  
M. Foster,<sup>‡,§</sup> and Bartosz Protas<sup>\*,†</sup>

<sup>†</sup>*Department of Mathematics and Statistics, McMaster University, Hamilton, Ontario,  
Canada L8S 4K1*

<sup>‡</sup>*The Faraday Institution, Quad One, Becquerel Avenue, Harwell Campus, Didcot, OX11  
0RA, United Kingdom*

<sup>¶</sup>*Department of Chemistry, McMaster University, Hamilton, Ontario, L8S 4L8, Canada*

<sup>§</sup>*School of Mathematics and Physics, University of Portsmouth, Lion Terrace, PO1 3HF,  
United Kingdom*

E-mail: bprotas@mcmaster.ca\*

## Abstract

Most mathematical models of the transport of charged species in battery electrodes require a constitutive relation describing intercalation of Lithium, which is a reversible process taking place on the interface between the electrolyte and active particle. The most commonly used model is the Butler-Volmer relation, which gives the current density as a product of two expressions: one, the exchange current, depends on Lithium concentration only whereas the other expression depends on both Lithium concentration and on the overpotential. We consider an inverse problem where an optimal form

of the exchange current density is inferred, subject to minimum assumptions, from experimental voltage curves. This inverse problem is recast as an optimization problem in which the least-squares error functional is minimized with a suitable Sobolev gradient approach. The proposed method is thoroughly validated and we also quantify the reconstruction uncertainty. Finally, we identify the universal features in the constitutive relations inferred from data obtained during charging and discharging at different C-rates and discuss how these features differ from the behaviour predicted by the standard Butler-Volmer relation. We also identify possible limitations of the proposed approach, mostly related to uncertainties inherent in the material properties assumed known in the inverse problem. Our approach can be used to systematically improve the accuracy of mathematical models employed to describe Li-ion batteries as well as other systems relying on the Butler-Volmer relation.

## 1 Introduction

The modelling of many physical processes relies on fundamental understanding of the interface between two interacting materials (or phases). It may also require the knowledge of specific material properties, which can be challenging to obtain or measure.<sup>1</sup> Interfacial models can be complex due to the coupling of different physical processes at the interface which makes probing their parametric dependence more difficult. In an effort to aid in the parametrization challenge, we propose an inverse modelling technique to optimally reconstruct constitutive relationships describing an important class of interfacial processes from data. Inverse modelling is an approach used to learn optimal forms of material properties from data by combining a mathematical model of the system with experimental measurements.

The present work proposes a computational approach alternative to machine learning techniques which have recently become popular.<sup>2-4</sup> Instead, we use tools from calculus of variations to design a numerical procedure to recover an optimal form of the constitutive re-

lation, where “optimal” means that the reconstructed constitutive relation achieves the best possible fit to the data. Such methods have already proved useful for solving a range of inverse problems in electrochemistry, which is an area abounding with systems whose material properties are notoriously difficult to measure directly.<sup>1,5-10</sup> Many of these applications are driven by recent advances in the mathematical modelling of transport processes in Lithium-ion (Li-ion) batteries, which are crucial to the development of electric vehicles and customer electronics.<sup>11,12</sup> While most of the work on inverse modelling in electrochemistry has focused on inferring material properties defined in the bulk of the electrolyte or active material, we extend this approach to constitutive relations characterizing interfacial phenomena. More specifically, we focus on constitutive relations describing the intercalation of ions from the electrolyte into the active material, which play a central role in modelling electrochemical systems,<sup>13</sup> but also find applications in other area of chemistry and physics as well as in biology. For example, such interfacial models have been used to relate the current density to the overpotential in bio-anode polarization curve,<sup>14</sup> to calculate the reaction rate from voltammograms,<sup>15</sup> to describe the electrode dynamics in supercapacitors,<sup>16</sup> and to describe the electrochemistry of a neuron.<sup>17</sup>

An inverse problem is usually formulated to minimize the least-squares error between the values predicted by the model and the experimentally measured quantities. When studying a distributed system (with dependence on space and/or time) and when the reconstructed property is a function, rather than a set of scalars, there are two main types of inverse problems. In the more traditional problems, the reconstructed material property is assumed to be a function of *independent* variables, usually space coordinate and/or time.<sup>18-20</sup> On the other hand, in less standard modern inverse problems,<sup>6,9,10,21-23</sup> the inferred properties are functions of the *dependent* variables in the system. The interfacial inverse problem we consider here belongs to this second category.

Inverse problems tend to be ill-posed, as they usually do not admit a unique exact solution, but rather a large number (often infinite) of approximate solutions.<sup>19</sup> Variation in

experimental measurements together with weak dependence of the model on some parameters can result in significant changes in the reconstructed solution which can be amplified by experimental and numerical errors. Yet, inverse modelling can help to elucidate optimal forms of constitutive relations and assess the validity of different models, as solutions violating thermodynamic principles can point to potential inconsistencies in the models used.<sup>7,9</sup>

The structure of the paper is as follows: in the next section we discuss the Butler-Volmer model; in Section 3, the experimental setup and the measurement data are introduced; Section 4 details the mathematical framework and optimization approach, and outlines the sensitivity analysis; the reconstruction results obtained with the inverse modelling approach are presented in Section 5; and finally, the conclusions of this work are presented in Section 6, whereas some additional technical material is collected in three appendices.

## 2 The Butler-Volmer Relation and its Generalization

Below we state the Butler-Volmer relation in a form that is commonly used, whereas the multiplicity of forms in which this relation is encountered is discussed in a recent review.<sup>24</sup> A complete derivation of the Butler-Volmer relation can be found in the literature.<sup>13,25,26</sup> Hereafter, the subscripts/superscripts “s” and “e” will denote quantities defined in the solid phase and in the electrolyte, respectively.

The net current density  $j$  is the difference between the backward and forward current densities at the interface, and the dependence of this quantity on electrochemical and thermodynamic parameters is given by the Butler-Volmer relation

$$j = Fk_0c_e^{\alpha_{a,m}}(c_{s,i,\max} - c_{s,i})^{\alpha_{a,m}}c_{s,i}^{\alpha_{c,m}}\left[e^{\frac{\alpha_{a,m}F}{RT}\eta} - e^{\frac{-\alpha_{c,m}F}{RT}\eta}\right], \quad \text{where} \quad \eta = \phi_s - \phi_e - U_{\text{eq}}^i(c_{s,i}), \quad (1)$$

in which  $\eta$  is the overpotential,  $c_{s,i}$  and  $c_e$  are the Lithium concentrations in the solid phase

and in the electrolyte with  $i = a, c$  indicating the anode or cathode respectively,  $\phi_s$  and  $\phi_e$  are the potentials in the solid phase and in the electrolyte (both measured with respect to a Li reference electrode), whereas  $U_{\text{eq}}^i(c_{s,i})$  is the concentration-dependent equilibrium potential of the electrode,  $\alpha_{a,m}$  and  $\alpha_{c,m} = 1 - \alpha_{a,m}$  are the anodic and cathodic charge transfer coefficients with  $m = -, +$  indicating the anode or cathode respectively (we do not use  $a$  and  $c$  here to avoid repeated identical indices),  $k_0$  is the reaction rate constant, and  $c_{s,i,\text{max}}$  is the maximum Lithium concentration in the solid. As is evident from (1), the Butler-Volmer relation can be naturally split into an algebraic factor depending on the Lithium concentration only, typically referred to as the exchange current, and the remaining exponential factor depending on both the potential difference  $\Delta\phi = \phi_s - \phi_e$  and the Lithium concentration in the electrolyte, the latter dependence through the equilibrium potential  $U_{\text{eq}}^i(c_{s,i})$ . This allows us to factor the Butler-Volmer relation (1) as

$$j = i_0(c_{s,i}) \psi(\Delta\phi, c_{s,i}), \quad \text{where} \quad (2a)$$

$$i_0(c_{s,i}) = Fk_0c_e^{\alpha_{a,m}} (c_{s,i,\text{max}} - c_{s,i})^{\alpha_{a,m}} c_{s,i}^{\alpha_{c,m}}, \quad (2b)$$

$$\psi(\Delta\phi, c_{s,i}) = \exp\left[\frac{\alpha_{a,m}F}{RT} (\Delta\phi - U_{\text{eq}}^i(c_{s,i}))\right] - \exp\left[-\frac{\alpha_{c,m}F}{RT} (\Delta\phi - U_{\text{eq}}^i(c_{s,i}))\right]. \quad (2c)$$

While the exponential term (2c) has had a long and well-documented history in electrochemistry,<sup>25–27</sup> additional assumptions are required to justify the form of the concentration-dependent algebraic factor (2b).<sup>24</sup> As will be discussed in more detail below, we focus on the dependence of the exchange current on  $c_{s,i}$  and its dependence on  $c_e$  in (2b) will be omitted so that our results are most applicable to situations in which the electrolyte concentration is approximately uniform (e.g., at relatively low currents or for thin electrodes).

In the present study, we thus consider a generalization of the Butler-Volmer relation (2) given

$$j = \iota(c_{s,i}) \psi(\Delta\phi, c_{s,i}), \quad (3)$$

where  $\psi(\Delta\phi, c_{s,i})$  is assumed known and given by (2c), whereas the factor  $i_0(c_{s,i})$ , cf. (2b), is replaced by a general function  $\iota(c_{s,i})$  whose optimal (in a mathematically precise sense to be specified below) form will be inferred from standard electrochemical measurements. This inverse problem will be solved using a computationally robust and thermodynamically consistent numerical optimization procedure where optimal functional forms of the factor  $\iota(c_{s,i})$  will be sought in a very general form subject to minimum only assumptions. These assumptions are:<sup>28</sup>

- A1. the function  $\iota = \iota(c_{s,i})$  must be sufficiently smooth (this will be made precise in Section 4.2),
- A2. when the Lithium concentration in the electrode goes to zero ( $c_{s,i} \rightarrow 0$ ), the Lithium flux out of the active material must vanish to prevent nonphysical negative Lithium concentrations in the electrode, and
- A3. when the electrode is saturated ( $c_{s,i} \rightarrow c_{s,i,\max}$ ), the Lithium flux into the active material must also vanish to prevent nonphysical overfilling of Lithium.

These represent constraints on the behaviour of the factor  $\iota(c_{s,i})$  for small ( $c_{s,i} \rightarrow 0$ ) and large ( $c_{s,i} \rightarrow c_{s,i,\max}$ ) concentrations. We note that this limiting behaviour is identical as in the standard Butler-Volmer model, cf. (2b). However, since the equilibrium potential  $U_{\text{eq}}^i(c_{s,i})$  is unbounded in these limits, cf. Supporting Information (Appendix A), the minimum and maximum concentrations of 0 and  $c_{s,i,\max}$  are in practice never attained.<sup>28</sup> Application of the proposed approach to voltage measurements performed during charge and discharge experiments produces optimal forms of the exchange current  $\iota(c_{s,i})$ , which are consistent between charge and discharge and reveal features making them quite different from expression (2b). We also characterize the uncertainty of the reconstructions and compare our results to a simpler approach where the inverse problem is solved by calibrating a small number of scalar parameters in expression (2b).

### 3 Experimental Datasets

In the formulation of our inverse problem, we will use several datasets from experiments performed on Li-ion batteries under galvanostatic conditions during both charge and discharge at different rates.<sup>29,30</sup> Below, we first describe the two experimental setups we considered and present the data obtained. Then, we demonstrate that, for all datasets, the fraction of the signal (the time-dependent voltage) containing information about the interfacial reactions is sufficiently large both to be used in inverse modelling and for the main assumptions underlying our mathematical model to be satisfied. Within the electrolyte, there is a potential drop between the anode and the cathode, which is accounted for when solving the complete Doyle-Fuller-Newman (DFN) model.<sup>13</sup> However, this potential drop is often either neglected in the standard Single-Particle model (SPM), cf. Section 4.1, based on the assumption that it is small when compared to the contributions from the electrode kinetics or is accounted for through a linearized model based on the assumption that the electrolyte can be considered ohmic if the current is small.<sup>10,31</sup> The SPM is typically an accurate reduction of the DFN model for C-rates up to approximately  $1C^{10}$  and given this well-known limitation of the SPM, we focus here on small and moderate charge/discharge rates only.

In order to assess whether the experimental datasets are consistent with the SPM, we determine the corresponding time-dependent concentration and potential profiles in the cells based on solutions of the complete DFN model<sup>13</sup> which are obtained using the suite Dan-deLiion.<sup>32</sup> This allows us to determine the relevant voltage drops for each component of the cell. Since the potential drop across the electrolyte is a function of both space (i.e., the distance  $x$  from the anode) and the (dis)charge time, we first compute the total drop as  $\phi_e(L, t) - \phi_e(0, t)$ , where  $L$  is the total length of the cell thereby taking a maximal estimate of the potential drop across the electrolyte, and then take the time average.

### 3.1 Slow Charge Rates

For slow charge rates, we consider two datasets corresponding to C-rates of C/10 and C/3. These datasets were obtained using an electrochemical cell constructed from an unused commercial Lithium-ion battery containing a double-sided coated graphite anode and  $\text{LiNi}_{0.6}\text{Mn}_{0.2}\text{Co}_{0.2}\text{O}_2$  (NMC622) cathode.<sup>29</sup> The commercial battery was disassembled, the electrodes were washed, cut, and dried, and reassembled in a replaceable cartridge-like battery container that mimics the single-layer pouch cell configuration. The assembled cell consists of a copper (Cu) current collector plate, graphite anode, Celgard 2325 separator, NMC622 cathode, and an aluminum (Al) current collector plate. The assembled cell was rested for 24 hours before being subject to cycling protocols and experimental measurements. Figure 1 shows each individual component of the cell before assembly. Full experimental details and set up can be found by Sanders et al.<sup>29</sup>



Figure 1: Image of the cell assembly. From left to right: bottom part of the cartridge with copper (Cu) metal current collector plate, graphite anode, Celgard 2325 separator, NMC622 cathode, and top part of the cartridge with aluminum (Al) current collector plate. The EPDM o-ring used to provide a gas-tight seal and 8 M2 PEEK screws used to close the cartridge are also shown around the top part on the right-hand side.

In Figure 2, the experimental voltage curves for the anode and cathode equilibrium voltages are plotted against the normalized concentration in the two electrodes. The graphite voltage curve in Figure 2a was obtained by charging a half-cell with a graphite electrode to the maximum voltage at a rate of C/140. The voltage curve for the NMC622 electrode in



Figure 2b was obtained by charging a half-cell with an NMC622 electrode to 4.2V at a rate of C/140. These measurements will be used as the equilibrium potentials in our model. The voltage curves obtained with the C-rates of C/10 and C/3 will be shown in Section 5 where we discuss our results.

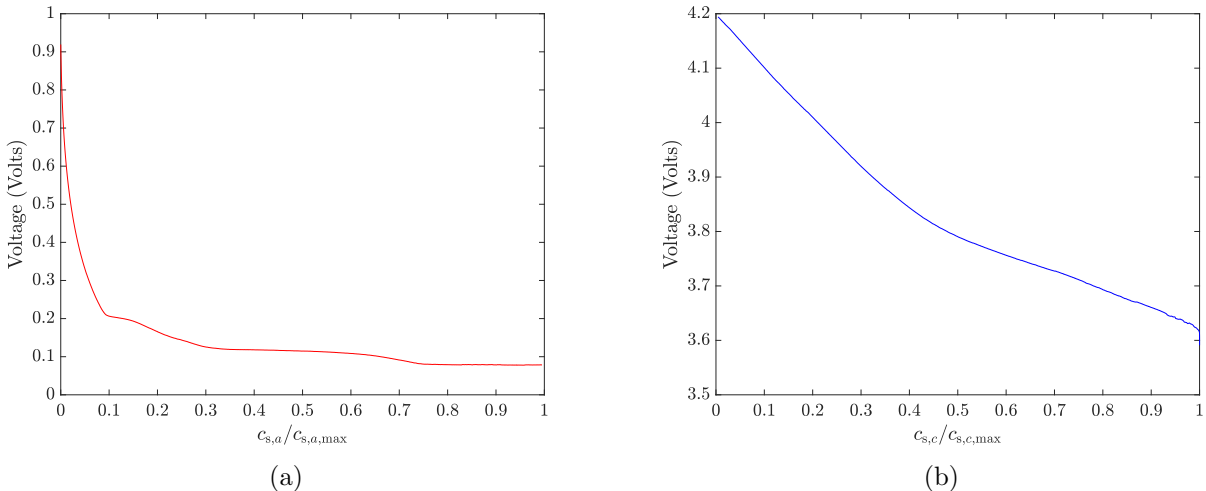


Figure 2: The equilibrium voltage curve for (a) the graphite anode and (b) for the NMC622 cathode in the cell used in the experiments described in Section 3.1.<sup>29</sup>

Table 1 details the percentage breakdown of the time-averaged voltage drops obtained by solving numerically the complete DFN model using the material parameters listed in Tables 5 and 6 in Supporting Information (Appendix C.1). In all cases, the overpotentials  $\eta_a$  and  $\eta_c$  have approximately the same share of the total potential as the time-averaged drop across the electrolyte. Table 1 also shows the ratios between the different potential drops corresponding to the two C-rates considered. We see that for all potential drops (except for  $V_c - V_a$ , as expected) these ratios are close to the ratio of the two C-rates, which is 10/3, confirming that the response is close to linear at small C-rates.

### 3.2 Moderate Discharge Rates

Experimental data for discharge rates of C/2 and 1C were obtained from Chen et al.<sup>30</sup> Their experiments utilized a cylindrical LG M5021700 (LGM50) cell containing an  $\text{LiNi}_{0.8}\text{Mn}_{0.1}\text{O}_1$

Table 1: Percentage breakdowns of the time-averaged potential drops corresponding to the main components of the cell used in the experiments described in Section 3.1.<sup>29</sup> The results were obtained by solving the complete DFN model using the material parameters listed in Tables 5 and 6 in Supporting Information (Appendix C.1).

Charge rate	$V_c - V_a$	$\eta_a$	$\eta_c$	Electrolyte
C/10	99.1755	0.2368	0.3344	0.2533
C/3	97.1927	1.0208	1.0195	0.7670
Ratio				
C/3:C/10	0.9800	4.3103	3.0492	3.0281

(NMC811) cathode and a graphite anode. A commercial cell was taken apart and assembled into two half cells to characterize the respective electrode and cell parameters. The obtained electrodes were then assembled into a three-electrode full cell configuration with a Celgard 2325 separator and subjected to cycling protocols under a variety of environments. Details can be found in the work by Chen et al.<sup>30</sup>

Table 2 details the percentage breakdown of the time-averaged voltage drops associated with the main components of the cell which were obtained by solving numerically the complete DFN model using the material parameters listed in Tables 7 and 8 in Supporting Information (Appendix C.2). Table 2 also shows the ratios between the different potential drops corresponding to the two C-rates considered. We see that when the C-rate increases from C/2 to 1C, these ratios are approximately 2 for all potential drops (except for the equilibrium potential  $V_c - V_a$ , as expected), which is consistent with the linear behaviour expected at low C-rates. Chen et al.<sup>30</sup> also obtained results at a higher discharge rate of 2C, but since this regime is outside the range of validity of the SPM, we will not consider this data in our study.

We remark that some experiments have made use of thin electrodes to ensure that the potential drop in the electrolyte is negligible.<sup>33,34</sup> In our case, we emphasize that in both the slow and moderate charge/discharge rate data we see a non-negligible potential drop in the electrolyte, which is on the order of the contributions from overpotentials  $\eta_a$  and  $\eta_c$ , cf. Tables 1 and 2. Thus, an SPM with a simple ohmic model accounting for the electrolyte

Table 2: Percentage breakdowns of the time-averaged potential drops corresponding to the main components of the cell used in the experiments described in Section 3.2.<sup>30</sup> The results were obtained by solving the complete DFN model using the material parameters listed in Tables 7 and 8 in Supporting Information (Appendix C.2).

Charge rate	$V_c - V_a$	$\eta_a$	$\eta_c$	Electrolyte
C/2	97.2504	1.5916	0.1907	0.9674
1C	94.8758	2.6239	0.4245	2.0758
Ratio				
1C:C/2	0.9756	1.6486	2.2262	2.1459

as discussed in the next section will be suitable for our purposes.

## 4 Mathematical Model

In this section, we first introduce the SPM framework, then formulate our inverse problem, describe its numerical solution, and finally discuss the sensitivity analysis. The SPM framework relies on several simplifying assumptions used to describe the construction of the Li-ion battery. Namely, the microstructure of the cell in each electrode is represented in terms of a representative spherical particle, the electrodes are spatially homogeneous and the intercalation reaction is uniform across the electrode.<sup>13,35,36</sup> In practice, these assumptions may not reflect the true behaviour of the cell. For example, during the manufacturing process, the active particles are usually covered with binder containing carbon and therefore active material may not be in a direct contact with the electrolyte.<sup>37,38</sup> Electrodes are typically produced with spatial inhomogeneities such that not all particles undergo intercalation at the same rate.<sup>39,40</sup> In addition, the electrode particles are not strictly spherical, which can lead to preferential intercalation in some parts of the electrode.<sup>41,42</sup> We note here that some of these limitations can be circumvented by employing idealized nonporous geometries.<sup>43-47</sup> However, the aforementioned assumptions are generally invoked when modelling cells under low-power operation (generally up to a C-rate of 1C).<sup>10,28,31,48,49</sup> We add that in our study the standard SPM is augmented to include an Ohmic potential drop in the electrolyte and features concentration-dependent diffusivity describing transport in the active particles. As

indicated in Section 3, the experimental data utilized in this work is within the realm of validity for this model.

## 4.1 Single Particle Model (SPM)

A standard description of the transport of Lithium in battery electrodes usually relies on the DFN model.<sup>13,35,36</sup> However, this model is computationally expensive and involves a large number of material parameters, which makes it difficult to calibrate. Both of these issues are partially alleviated by various simplified models such as the SPM, which assumes that the electrode particles are uniformly distributed spheres and that electrochemical reactions are uniform throughout the electrode.<sup>31</sup> These assumptions reduce the model to a transport problem in a single representative particle. The SPM can be derived as a certain asymptotic limit of the DFN model and the price to be paid for its simplicity is that it is valid for small C-rates only — it is usually assumed that it does not provide an accurate description beyond 1C.<sup>10,28,31,48,49</sup> In our study, a suitably modified SPM is applied to describe transport both in the anode and the cathode.

In the SPM, the Lithium transport in the solid state is described by a nonlinear diffusion equation written in spherical coordinates<sup>13,35,36</sup>

$$\frac{\partial c_{s,i}}{\partial t} = \frac{1}{r^2} \frac{\partial}{\partial r} \left[ D_s(c_{s,i}) r^2 \frac{\partial c_{s,i}}{\partial r} \right] \quad \text{in } (0, R_i) \times (0, t_f], \quad (4)$$

where  $r$  measures the radial distance from the center of the particle outward to the particle's surface at  $R_i$ ,  $D_s(c_{s,i})$  is the (concentration-dependent) diffusivity in the electrodes,  $t$  is time ranging from 0 to the final time  $t_f$ , and  $i = a, c$  corresponds to the anode and cathode,

respectively. The accompanying boundary conditions are

$$\left. \frac{\partial c_{s,i}}{\partial r} \right|_{r=0} = 0 \quad \text{in } (0, t_f], \quad (5)$$

$$-D_s(c_{s,i}) \left. \frac{\partial c_{s,i}}{\partial r} \right|_{r=R_i} = \frac{j_i}{F} \quad \text{in } (0, t_f], \quad (6)$$

where  $F$  is the Faraday constant, and the initial condition is

$$c_{s,i}|_{t=0} = c_{s,i;0}, \quad (7)$$

where  $c_{s,i;0}$  is the initial concentration of Lithium in the solid. Given that transport in the electrolyte is not explicitly modelled in the SPM, the current density  $j_i$  in the boundary condition (6) can be deduced directly from the total current  $I(t)$  applied to the cell. The conservation of charge at the anode and cathode implies

$$4\pi R_i^2 j_i = \pm \frac{I(t)}{n_i}, \quad (8)$$

in which the total number of particles in the electrode is given by  $n_i = A_i L_i \epsilon_i / (4/3\pi R_i^3)$ , where  $A_i$  is the cross-sectional area of the electrode,  $L_i$  is the thickness of the electrode, and  $\epsilon_i$  is the volume fraction in the electrode. The right-hand side is positive for  $i = a$  and negative for  $i = c$ . Finally, the total current to the cell is  $I(t)$ , with  $I(t) < 0$  for the anode during charging,  $I(t) > 0$  for the cathode during charging, and vice versa during discharging. Relation (8) ensures that there is enough (de)intercalation reaction to meet the current demand. We emphasize that, while the Butler-Volmer relation (2) is not used in the solution of the solution of the SPM, it is required in order to determine the corresponding overpotential  $\eta$  which is done by post-processing the solution of the SPM. This property will be the basis for the inverse problem introduced in the next section.

Since in our experimental data the potential drop in the the electrolyte is of approximately the same magnitude as the overpotentials (cf. Tables 1 and 2), we augment the expression

for the total potential drop predicted by SPM with a term representing the potential drop in the electrolyte which is assumed to be ohmic<sup>50</sup> and proportional to the applied current  $I$  via a constant resistivity  $R_{el}$ . This assumption is supported by the data in Tables 1 and 2 which indicate that the potential drop in the electrolyte does increase approximately linearly with the applied current. The total potential drop predicted by the model thus takes the form

$$V_{cell} = U_{eq}^c(c_{s,c}|_{r=R_c}) - U_{eq}^a(c_{s,a}|_{r=R_a}) + \eta_c - \eta_a + R_{el}I, \quad (9)$$

where the additional subscripts  $a$  and  $c$  denote anode and cathode, respectively. Relation (9) will serve as the basis for the inverse modelling introduced in Section 4.2. We note that the SPM is usually defined through (4)–(8) and will refer to the model resulting from the inclusion of relation (9) as an “augmented” SPM.

## 4.2 Inverse Problems

Solution of the SPM given above yields concentration profiles  $c_{s,i}(t)$  as functions of time  $t$ . Within the SPM (4)–(8), the concentration  $c_{s,i}(t)$  does not depend on the constitutive relation (3), however, the corresponding overpotential does. The idea behind the inverse problems is thus to infer the optimal form of the factor  $\iota(c_{s,i})$  by minimizing the discrepancy between the overpotential predicted by (3) and the overpotential deduced from the experimental data. The total potential measured experimentally as discussed in Section 3 will be denoted  $\bar{V}_{cell}(t)$ .

In our first, simpler, inverse problem we assume the constitutive relation is given by the Butler-Volmer equation (2) and calibrate the scalar parameters  $\alpha_{a,m}$  and  $k_0$  parameterizing this relation for both the anode and the cathode as well as the electrolyte resistivity  $R_{el}$  in (9). Since the total potential is dominated by contributions from the equilibrium potentials,

cf. relation (9) and Tables 1–2, we consider the following error functional

$$\mathcal{J}_1 = \frac{1}{2} \int_0^{t_f} [\Delta\eta(t) - \Delta\bar{\eta}(t)]^2 dt, \quad (10)$$

where  $\Delta\eta(t) = \eta_c(t) - \eta_a(t) + R_{el}I(t)$  and  $\Delta\bar{\eta}(t) = \bar{V}_{cell}(t) - [U_{eq}^c(c_{s,c}|_{r=R_c}) - U_{eq}^a(c_{s,a}|_{r=R_a})]$  in which  $\eta_a(t)$  and  $\eta_c(t)$  are obtained by inverting relation (1) defined on the anode and the cathode (each of these relations depends on the parameters  $\alpha_{a,m}$  and  $k_0$ ), whereas  $c_{s,a}$  and  $c_{s,c}$  are the solutions of system (4)–(8) obtained at the two electrodes (additional information how  $\mathcal{J}_1$  evaluated is provided in the next section). The error functional (10) is a least-square measure of the discrepancy between the portion of the total potential directly depending on the constitutive relation describing ion intercalation, and is therefore numerically better conditioned than a least-square measure of the difference  $V_{cell}(t) - \bar{V}_{cell}(t)$ . This leads to the finite-dimensional optimization problem

$$\text{P1: } [\hat{k}_{0,-}, \hat{\alpha}_{a,-}, \hat{k}_{0,+}, \hat{\alpha}_{a,+}, \hat{R}_{el}] = \underset{[k_{0,-}, \alpha_{a,-}, k_{0,+}, \alpha_{a,+}, R_{el}] \in \mathbb{R}^5}{\text{argmin}} \mathcal{J}_1(k_{0,-}, \alpha_{a,-}, k_{0,+}, \alpha_{a,+}, R_{el}),$$

where hats ( $\hat{\cdot}$ ) denote optimal values of the material parameters and subscripts  $-$  and  $+$  on  $k_0$  and  $\alpha_{a,m}$  denote quantities defined on the anode and the cathode, respectively.

In contrast to Problem P1 where we seek optimal parameters in relations (2) defined both on the anode and the cathode, in our main inverse problem, Problem P2, we will focus on inferring the optimal form of the factor  $\iota(c_{s,a})$  in the constitutive relation (3) on the anode only while assuming that on the cathode the constitutive relation has the standard form (2) with parameters  $\hat{k}_{0,-}$  and  $\hat{\alpha}_{a,-}$  obtained by solving Problem P1. Thus, the second error

functional is defined to measure the error in the overpotential on the anode as

$$\mathcal{J}_2 = \frac{1}{2} \int_0^{t_f} [\eta_a(t) - \bar{\eta}^{P2}(t)]^2 dt, \quad \text{where} \quad (11a)$$

$$\eta_a = \psi^{-1} \left( \frac{I}{F\iota(c_{s,a})} \right), \quad (11b)$$

$$\bar{\eta}^{P2}(t) = - \left[ \bar{V}_{cell}(t) - \left( U_{eq}^c(c_{s,c}|_{r=R_c}) - U_{eq}^a(c_{s,a}|_{r=R_a}) + \eta_c^{P1} + \widehat{R}_{el}I \right) \right], \quad (11c)$$

in which the superscript ‘‘P1’’ denotes quantities computed using information from the solution of Problem P1 and, with a slight abuse of notation,  $\psi^{-1}(\cdot)$  denotes the function  $\Delta\phi = \Delta\phi(c_{s,i})$  which is the solution of the equation  $I/(F\iota(c_{s,a})) - \psi(\Delta\phi(c_{s,a}), c_{s,a}) = 0$  for  $c_{s,a} \in [0, c_{s,a,max}]$ , cf. (3) (the existence of such a function is guaranteed by the implicit function theorem). This notation emphasizes the dependence of the expression in (11b) on the factor  $\iota(c_{s,a})$  in the constitutive relation (3) describing ion intercalation in the anode. As stipulated by assumptions A1–A3 in Section 2, see also Supporting Information (Appendix A), we must require the function  $\iota(c_{s,a})$  to vanish at both vanishing and maximum concentrations, i.e., for  $c_{s,a} = 0$  and for  $c_{s,a} = c_{s,a,max}$ . We also need the function  $\iota(c_{s,a})$  to be continuous with square-integrable (distributional) derivatives, such that it will belong to the Sobolev space<sup>51</sup>  $H_0^1([0, c_{s,a,max}])$  (the subscript ‘‘0’’ indicates that functions belonging to this space vanish at the boundary). The optimal functional form of the exchange current  $\iota(c_{s,a})$  on the anode can then be obtained as a solution of the optimization problem

$$\text{P2:} \quad [\widehat{\iota}(c_{s,a})] = \underset{\iota(c_{s,a}) \in H_0^1([0, c_{s,a,max}])}{\text{argmin}} \quad \mathcal{J}_2(\iota(c_{s,a})),$$

where the corresponding constitutive relation (3) takes the optimal form  $\widehat{j}(c_{s,a}) = \widehat{\iota}(c_{s,a})\psi(\Delta\phi, c_{s,a})$ .

We note that the framework outlined above could also be utilized to reconstruct the optimal form of the exchange current on the cathode. In this case, the cost functional (11) would include  $\eta_c(t)$ , equation (11b) would involve  $\eta_c$  as a function of  $\iota(c_{s,c})$  whereas equation (11c)



would use  $\eta_a^{P1}$  (with a correction to the sign on the right-hand side, cf. equation (9)). In such case the optimal form of the constitutive relation would be  $\widehat{j}(c_{s,c}) = \widehat{\iota}(c_{s,c})\psi(\Delta\phi, c_{s,c})$ , cf. (3). Moreover, one could solve these two problems iteratively making it possible to refine the reconstructions of the exchange current on both electrodes. Our approach to solving Problems P1 and P2 is described next.

### 4.3 Computational Approach

Evaluation of the error functionals (10) and (11) requires solution of the SPM, cf. (4)–(9), which is done using a standard finite element method.<sup>10,32</sup> Problem P1 represents unconstrained minimization over  $\mathbb{R}^5$  and is solved numerically in a straightforward manner using the function `fminunc` in MATLAB. The key step is evaluation of the error functional (10) and the procedure is outlined in Algorithm 1.

---

**Algorithm 1** Evaluation of the error functional  $\mathcal{J}_1$  in the solution of Problem P1

---

**Input:**

$\overline{V}_{\text{cell}}(t)$  — experimental voltage as a function of time

$k_{0,-}^o, k_{0,+}^o$  — initial guesses for reaction rate for anode and cathode

$\alpha_{a,-}^o, \alpha_{a,+}^o$  — initial guesses for transfer coefficients for anode and cathode

$R_{el}^o$  — initial guess for electrolyte resistance

**Output:**  $\mathcal{J}_1(k_{0,-}, k_{0,+}, \alpha_{a,-}, \alpha_{a,+}, R_{el})$

---

Solve the SPM equations (4)–(8) for  $c_{s,a}$  and  $c_{s,c}$

Compute  $\Delta\bar{\eta}(t) = - \left[ \overline{V}_{\text{cell}}(t) - \left( U_{\text{eq}}^c(c_{s,c}|_{r=R_c}) - U_{\text{eq}}^a(c_{s,a}|_{r=R_a}) \right) \right]$

Compute  $\eta_a$  and  $\eta_c$  by inverting relations 1 and 8 with unknowns  $k_{0,-}, k_{0,+}, \alpha_{a,-}$ , and  $\alpha_{a,+}$

Compute  $\Delta\eta(t) = \eta_c - \eta_a + R_{el}I(t)$

Determine  $\mathcal{J}_1(k_{0,-}, k_{0,+}, \alpha_{a,-}, \alpha_{a,+}, R_{el})$  by evaluating the integral in (10)

---

Problem P2 represents minimization over an infinite-dimensional function space  $H_0^1$  and therefore requires a specialized approach. We compute the optimal exchange current using the discrete gradient flow as  $\widehat{\iota}(c_{s,i}) = \lim_{n \rightarrow \infty} \iota^{(n)}(c_{s,i})$  where the approximations  $\iota^{(n)}(c_{s,i})$  are

computed iteratively by

$$\begin{aligned}\iota^{(n+1)}(c_{s,i}) &= \iota^{(n)}(c_{s,i}) - \tau^{(n)} \nabla \mathcal{J}_2(\iota^{(n)}(c_{s,i})), \\ \iota^{(0)}(c_{s,i}) &= \iota_0(c_{s,i}),\end{aligned}\tag{12}$$

in which  $\iota_0(c_{s,i})$  is a suitable initial guess,  $\nabla \mathcal{J}_2(\iota^{(n)}(c_{s,i}))$  is the Sobolev gradient of the error functional (11) at the  $n$ th iteration, and  $\tau^{(n)}$  is the step size along the gradient direction. The initial guess  $\iota_0(c_{s,i})$  is chosen to vanish at  $c_{s,i} = 0$  and at  $c_{s,i} = c_{s,i,\max}$ , so that the same limiting behaviour will be inherited by the optimal solution  $\tilde{\iota}(c_{s,i})$ , provided the gradients  $\nabla \mathcal{J}_2(c_{s,i})$  also vanish at  $c_{s,i} = 0$  and  $c_{s,i} = c_{s,i,\max}$ , cf. Supporting Information (Appendix A). In practice, the initial guess  $\iota_0(c_{s,i})$  is taken as the factor  $i_0$  in the Butler-Volmer relation (2b) with optimal parameters found by solving Problem P1 which, by construction, ensures the correct behaviour at  $c_{s,i} = c_0, c_{s,i,\max}$ . Computation of the Sobolev gradient  $\nabla \mathcal{J}_2(\iota(c_{s,i}))$ , which is a key element of approach (12), is described in Supporting Information (Appendix B) and together with the properties of the initial guess  $\iota_0(c_{s,i})$  ensures the required smoothness of the optimal exchange current  $\tilde{\iota}(c_{s,i})$  and its correct behaviour at  $c_{s,i} = c_0, c_{s,i,\max}$ . The optimal step size in (12) is found by solving the line-minimization problem

$$\tau^{(n)} = \underset{\tau > 0}{\operatorname{argmin}} \mathcal{J}_2(\iota(c_{s,i}) - \tau \nabla^{H^1} \mathcal{J}_2(\iota(c_{s,i}))),\tag{13}$$

which is done conveniently using Brent's algorithm.<sup>52</sup> Expression (12) is evaluated using the collocation approach on the domain  $[0, c_{s,i,\max}]$  discretized with a uniform grid based on  $N = 500$  grid points. We also considered finer meshes, but they did not produce appreciable differences in the obtained results, hence the aforementioned resolution was used as a trade-off between accuracy and the computational cost. When determining the Sobolev gradients, one must specify the value of the Sobolev parameter  $0 < \ell < \infty$  which appears in the definition of the inner product (24) and determines the relative smoothness of the gradients. More specifically,  $\ell$  may be regarded as a characteristic, or cut-off, value of the concentration

below which all information in the gradient  $\nabla \mathcal{J}_2(\iota(c_{s,i}))$  is smoothed out. At the validation stage, values of  $\ell$  spanning several orders of magnitude were considered to determine the value resulting in the fastest rate of convergence of iterations (12). Based on these tests, we chose  $\ell = 3000000$  and  $\ell = 100000$  for the case of slow charge and moderate discharge rates, respectively. The steps leading to the solution of Problem P2 are summarized as Algorithm 2.

The computational approach was systematically validated by solving Problems P1 and P2 with “manufactured” measurement data. More specifically, we assumed a certain form of the constitutive relation ((2) with some values of  $\alpha_{a,m}$  and  $k_0$  for Problem P1 and (3) with some function  $\iota(c_{s,i})$  for Problem P2) which was used to generate measurements. The true constitutive relations were then reconstructed using Algorithm 2. Excellent reconstruction accuracy was achieved with errors essentially at the level of errors due to numerical discretization. We add that Problems P1 and P2 are non-convex and we have found some evidence for the presence of nonunique (local) minimizers when different initial guesses are used in Algorithms 1 and 2. However, in all instances these local minimizers involved physically inconsistent material properties (e.g., with incorrect signs), which made it easy to eliminate them. Analysis of the sensitivity of solutions to Problems P1 and P2 to perturbations of measurement data is discussed in the next section.

---

**Algorithm 2** Solution of Problem P2 using discrete gradient flow (12)

---

**Input:**

$\epsilon$  — tolerance

$\ell$  — Sobolev parameter

$\bar{V}_{\text{cell}}(t)$  — experimental voltage as a function of time

$k_{0,-}^o, k_{0,+}^o$  — initial guesses for reaction rate for anode and cathode

$\alpha_{a,-}^o, \alpha_{a,+}^o$  — initial guesses for transfer coefficients for anode and cathode

$R_{el}^o$  — initial guess for electrolyte resistance

**Output:**  $\hat{k}_{0,-}, \hat{k}_{0,+}, \hat{\alpha}_{a,-}, \hat{\alpha}_{a,+}, \hat{R}_{el}$ , and  $\hat{\iota}(c_{s,i})$

---

Solve Problem P1 using `fminunc`

Compute  $\bar{\eta}(t) \leftarrow - \left[ \bar{V}_{\text{cell}}(t) - \left( U_{\text{eq}}^c(c_{s,c}|_{r=R_c}) - U_{\text{eq}}^a(c_{s,a}|_{r=R_a}) + \eta_c^{P1} + \hat{R}_{el}I \right) \right]$

Set  $\iota_0(c_{s,i}) = F \hat{k}_{0,-} \hat{c}_e^{\hat{\alpha}_{a,-}} (c_{s,i,\text{max}} - c_{s,i})^{\hat{\alpha}_{a,-}} c_{s,i}^{(1-\hat{\alpha}_{a,-})}$

**repeat**

    Evaluate  $\nabla^{L^2} \mathcal{J}(\iota(c_{s,i}))$

    Compute  $\nabla^{H^1} \mathcal{J}(\iota(c_{s,i}))$  given  $\nabla^{L^2} \mathcal{J}(\iota(c_{s,i}))$

    Perform a Polak-Ribiere conjugate gradient update  $\nabla^{H^1} \mathcal{J}(\iota(c_{s,i}))$

    Find the step size  $\tau^{(n)}$  by solving the line-search problem (13) with Brent's method

$\iota^{(n+1)}(c_{s,i}) \leftarrow \iota^{(n)}(c_{s,i}) - \tau^{(n)} \nabla \mathcal{J}(\iota^{(n)}(c_{s,i}))$

**until**  $\frac{|\mathcal{J}(\iota^{(n)}(c_{s,i}))| - |\mathcal{J}(\iota^{(n-1)}(c_{s,i}))|}{|\mathcal{J}(\iota^{(n)}(c_{s,i}))|} < \epsilon$

---

## 4.4 Sensitivity Analysis

Inverse problems are generally ill-posed and variations in the experimental data can result in significant shifts in the reconstructed solutions.<sup>19</sup> To explore the effects of small perturbations in the experimental data on the solution of Problems P1 and P2, a Monte-Carlo analysis is developed where the measurement data is perturbed as

$$\hat{V}_{\text{cell}}(t) = V_{\text{cell}}(t) + \sum_{k=1}^3 \frac{a_k}{k^2} \sin\left(\frac{2\pi kt}{t_f}\right) + \sum_{k=1}^3 \frac{b_k}{k^2} \cos\left(\frac{2\pi kt}{t_f}\right), \quad t \in [0, t_f], \quad (14)$$

in which  $a_k$  and  $b_k$ ,  $k = 1, 2, 3$ , are normally distributed random variables with zero mean and a prescribed standard deviation. Problems P1 and P2 with measurement data perturbed as in (14) are then solved  $M$  times ( $M \gg 1$ ), each time using a different sample of the random variables  $a_k$  and  $b_k$ . This allows us to compute the statistics of the reconstruction errors and

of the optimal constitutive relations  $\hat{u}(c_{s,a})$  corresponding to perturbed measurements which provide information about their sensitivity to noise.

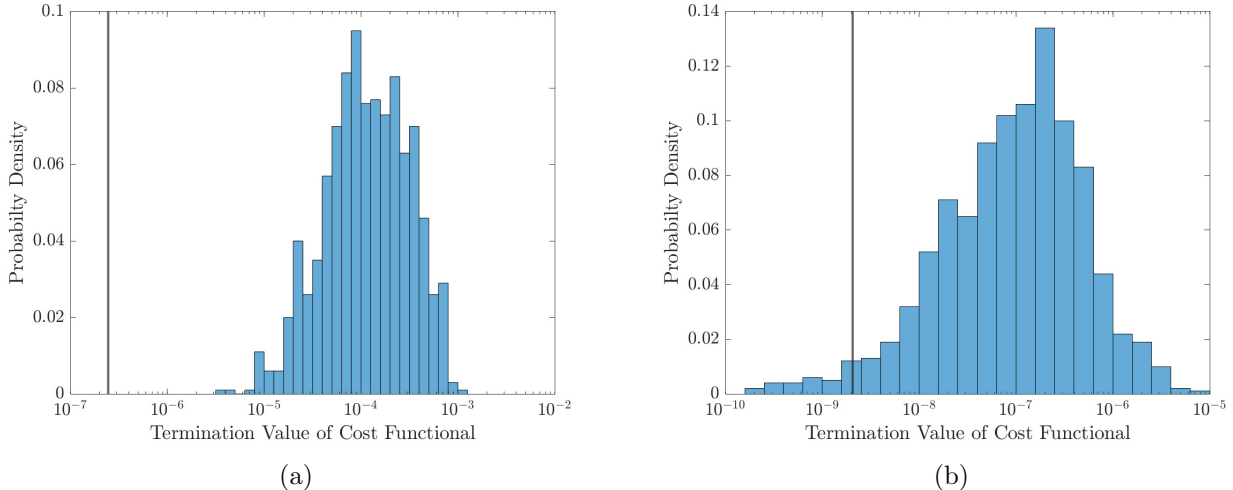


Figure 3: PDFs of the error functionals (a)  $\mathcal{J}_1$  and (b)  $\mathcal{J}_2$  obtained in Monte-Carlo sensitivity analysis. The vertical lines represent the values of  $\mathcal{J}_1$  and  $\mathcal{J}_2$  obtained in solutions of Problems P1 and P2 with no noise.

Our sensitivity analysis is then performed based on the manufactured measurement data at 1C (which was also used to validate Algorithm 2) and using  $M = 3000$  normally distributed noise samples with zero mean and 0.0025 standard deviation. Using the empirical 3-sigma rule,<sup>53</sup> the relative variation of the measurement data due to noise can be estimated as  $6 \times 0.0025/1.3 \approx 0.012$  or 1.2%, where 1.3 in the denominator is the approximate total voltage drop during the (dis)charge cycle. The effect of this noise is thus comparable to the potential drop in the electrolyte, cf. Tables 1 and 2, which is accounted for in the voltage (9) predicted by the augmented SPM. The probability density functions (PDFs) of the error functionals (10) and (11) obtained by solving Problems P1 and P2 with measurement data perturbed as described above are shown in Figure 3. The corresponding *mean* inferred exchange currents are shown in Figure 4 together with their 95% confidence intervals and the standard Butler-Volmer relation (1) with some reference parameter values that were used to “manufacture” the measurements. We observe that optimal reconstructions obtained by solving both Problem P1 and P2 capture the general functional form of the true constitutive

relation quite well, but the magnitude is off by a bit more than 10% even though the noise amplitude is rather small. It ought to be emphasized however that such level of uncertainty is not uncommon in parametrization of electrochemical systems.<sup>9,10</sup> The corresponding distributions of optimal anode overpotentials are shown in Figure 5 where deviations from the original data are rather small. We also mention that additional Monte-Carlo simulations were performed using the random coefficients  $a_k$  and  $b_k$  in (14) with several decreasing standard deviations and in this limit of vanishing noise amplitude, the deterministic solution is recovered, confirming the consistency of the calculations. These observations allow us to conclude that a modest amount of noise in the measurement data has some quantitative and little qualitative effect on the obtained reconstructions.

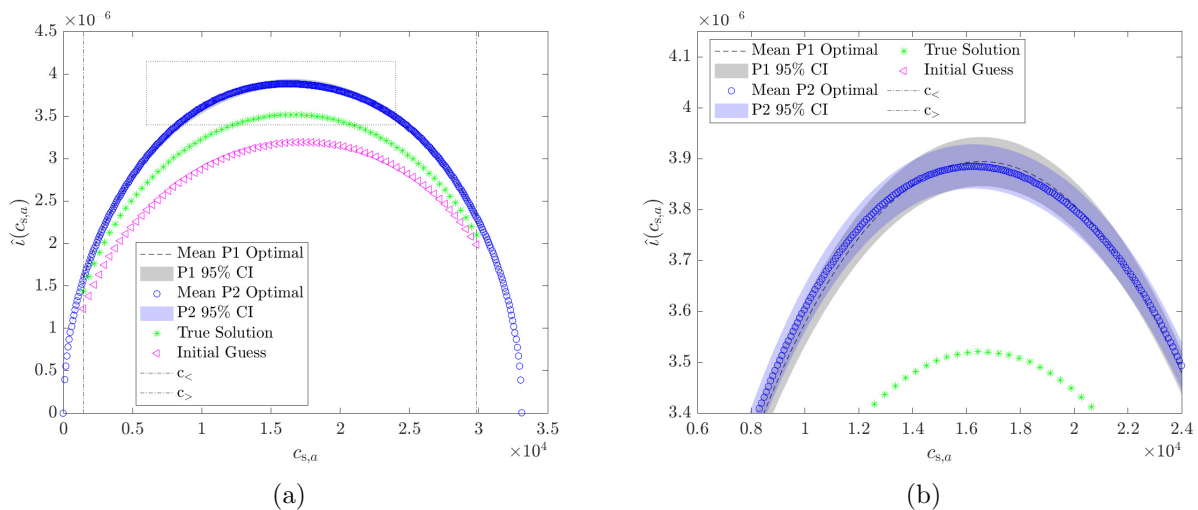


Figure 4: Optimal reconstructions of the exchange current (black dashed lines)  $i_0(c_s)$  and (blue circles)  $\hat{i}(c_{s,a})$  obtained by solving Problems P1 and P2 with measurement data perturbed as in (14) for (a) the entire concentration range and (b) intermediate concentrations indicated by the dotted box in (a). The shaded bands indicate the 95% confidence intervals whereas the vertical lines represent the bounds  $c_<$  and  $c_>$  of the identifiability interval  $\mathcal{I}$ . The true exchange current used to manufacture the measurements is shown in green.

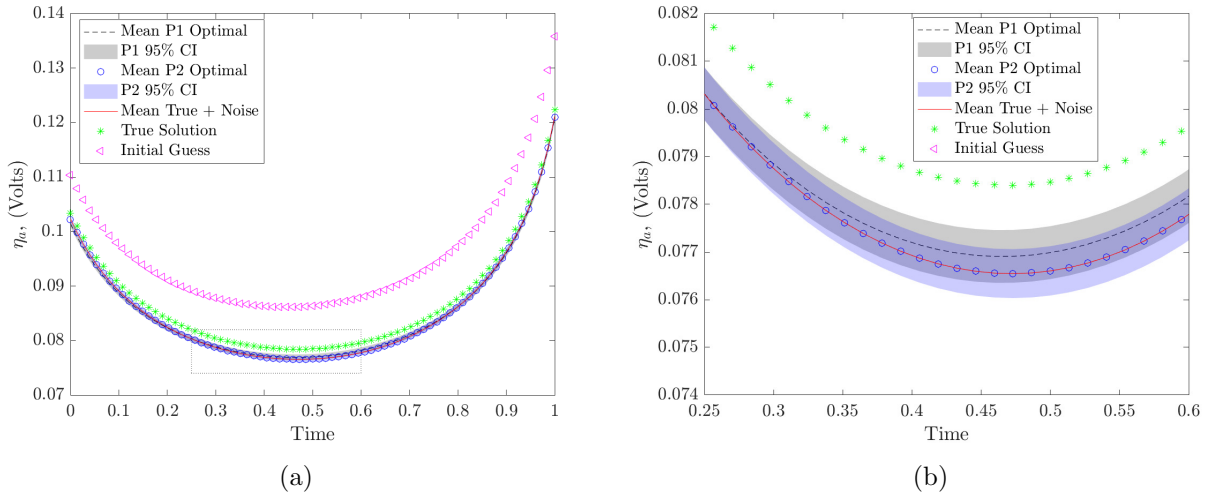


Figure 5: Anode overpotentials corresponding to the optimal exchange currents shown in Figure 4 for (a) the entire normalized time window and (b) magnification around intermediate times indicated by the dotted box in (a). The line types and colour-coding are the same as in Figure 4 with an added red solid line to represent the average value of the overpotential when the total potential is perturbed with noise.

## 5 Results

We compare the optimal constitutive relations reconstructed by solving Problems P1 and P2 using data for slow charge and moderate discharge rates against the standard form of the Butler-Volmer relation (1) for a graphite electrode. In the latter, we set  $\alpha_{a,m} = \alpha_{c,m} = 1/2$ , which is a standard choice for the transfer coefficients,<sup>13,26</sup> and in the problem with slow charge rates we set  $k_0 = 1.8742 \times 10^{-12}$  which is taken from a similar set-up of a graphite anode with an NMC622 cathode,<sup>54</sup> whereas in the problem with moderate charge rates we set  $k_0 = 6.72 \times 10^{-12}$  which was measured experimentally when collecting the data for a graphite anode with an NMC811 cathode.<sup>30</sup> Hereafter we will refer to these values of  $\alpha_{a,m}$ ,  $\alpha_{c,m}$  and  $k_0$  as “nominal”.

### 5.1 Slow Charge Rates

We first consider solutions of Problem P1 where scalar parameters are calibrated in expression (2b) before analyzing the results obtained by solving Problem P2 in which the exchange

current  $\iota(c_{s,a})$  is sought in a fairly general form. In Figure 6, we show the values of the error functional (10) corresponding to solutions of Problem P1 and see that compared to the values of  $\mathcal{J}_1$  obtained using the standard Butler-Volmer relation (1), they are reduced only mildly, by less than one order of magnitude for both C-rates. The solution to Problem P1 suggests that a small deviation from the standard functional form of the exchange current density already provides a relatively good fit.

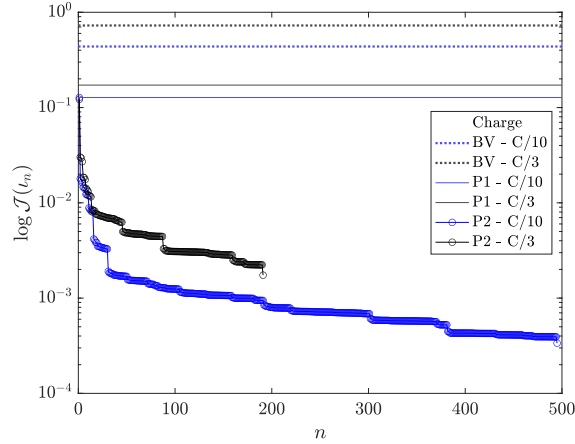


Figure 6: Cost functional  $\mathcal{J}_2$  as function of iterations in the solution of Problem P2 using Algorithm 2 at the C-rate of C/10 (blue lines with circles) and C/3 (black lines with circles). The horizontal lines represent the values of the error functional  $\mathcal{J}_1$  corresponding to the standard Butler-Volmer equation (1) (dotted lines) and the terminal values obtained in the solutions of Problem P1 at C-rates of C/10 (blue solid lines) and C/3 (black solid lines).

Table 3: Material parameters obtained by solving Problem P1.

Charge Rate	Parameter	Value
C/10	anode reaction rate constant, $\widehat{k}_{0,-}$	$1.076 \times 10^{-12}$
	cathode reaction rate constant, $\widehat{k}_{0,+}$	$4.416 \times 10^{-12}$
	anode anodic transfer coefficient, $\widehat{\alpha}_{a,-}$	0.5667
	cathodic anodic transfer coefficient, $\widehat{\alpha}_{a,+}$	0.4948
	electrolyte resistance, $\widehat{R}_{el}$	0.5813
C/3	anode reaction rate constant, $\widehat{k}_{0,-}$	$2.428 \times 10^{-12}$
	cathode reaction rate constant, $\widehat{k}_{0,+}$	$4.93 \times 10^{-12}$
	anode anodic transfer coefficient, $\widehat{\alpha}_{a,-}$	0.4999
	cathodic anodic transfer coefficient, $\widehat{\alpha}_{a,+}$	0.4959
	electrolyte resistance, $\widehat{R}_{el}$	0.5625

The material parameters inferred by solving Problem P1 are summarized in Table 3. We



see that the optimal parameter values obtained at the two C-rates are quite similar and from Figure 7, we see that the dependence on  $c_{s,a}$  is similar to the standard Butler-Volmer relation, but with a reduction in magnitude due to values of  $\widehat{k}_0$  being smaller by two orders of magnitude.

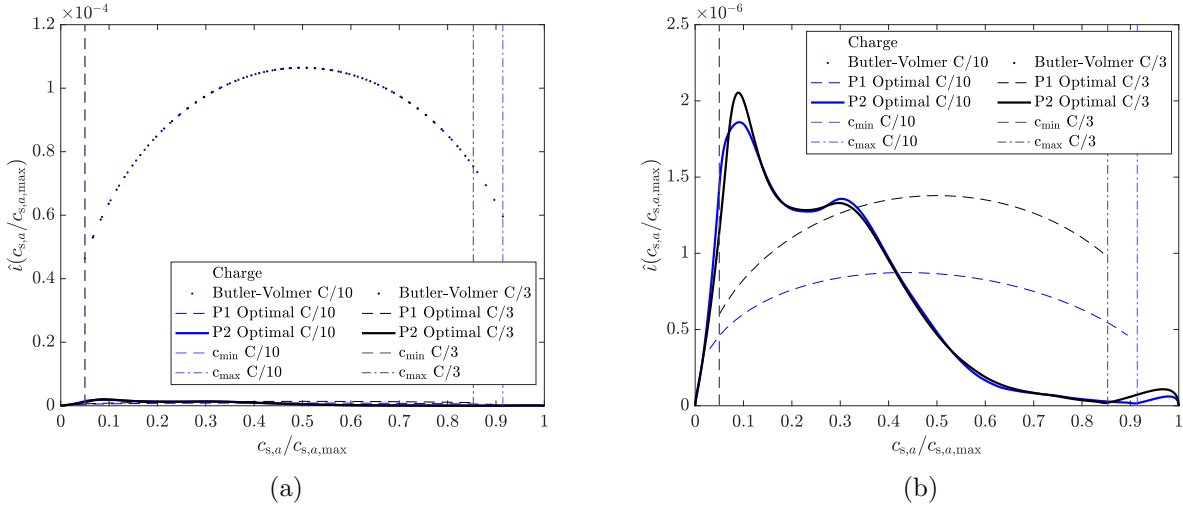


Figure 7: Optimal reconstructions of the exchange current obtained by solving Problem P1 (dashed lines) and Problem P2 (solid lines) as function of the normalized concentration  $c_s/c_{s,\max}$  for (a) the entire concentration range and (b) small values of the exchange current. Panel (a) also shows the standard Butler-Volmer relation (1) with the nominal parameter values (dotted lines), whereas the vertical lines represent the bounds of the identifiability intervals at the two C-rates.

The reconstructed overpotentials and the total cell potentials are compared as functions of time to the experimental data in Figure 8. While the anode overpotential corresponding to the Butler-Volmer relation with parameters calibrated by solving Problem P1, cf. Table 3, has values coinciding with a subset of the values observed in the actual measurements, its dependence on time  $t$  is incorrect. The same behaviour is also evident, though less pronounced due to the presence of large equilibrium potentials, in Figure 8b where we show the total potentials.

We now move on to discuss the results obtained by solving Problem P2. In Figure 6, we see that after a few hundred iterations in Algorithm 2, the value of the error functional  $\mathcal{J}_2$  is reduced by several orders of magnitude. The obtained optimal forms  $\widehat{i}(c_{s,a})$  of the exchange

current shown in Figure 7 are strikingly similar for both C-rates. The optimal solutions are skewed towards smaller concentrations where larger exchange currents are predicted, unlike solutions of Problem P1. In addition, they feature localized peaks at concentration values near the smallest resolved values. As was the case with solutions of Problem P1, the optimal functions  $\hat{i}(c_{s,a})$  inferred at the two C-rates are rather similar, except that the peak at low concentrations is steeper at the higher C-rate. Figure 8 shows that, as expected from the small errors evident in Figure 6, both the overpotentials and the total potentials predicted by the constitutive relation (3) with the optimal exchange currents  $\hat{i}(c_{s,a})$  shown in Figure 8 provide a better fit to the measured data.

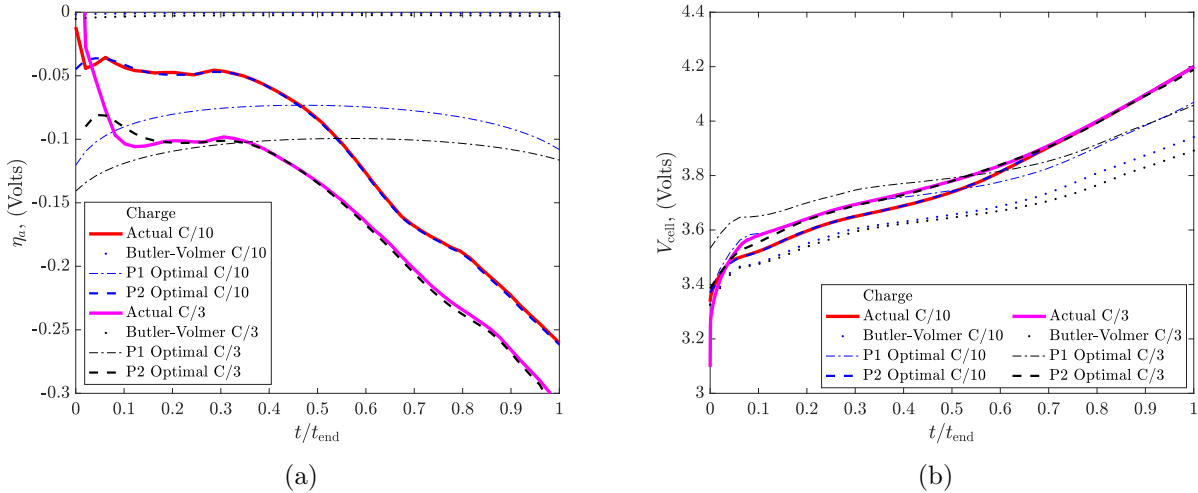


Figure 8: (a) Anode overpotentials and (b) total potentials predicted by the constitutive relation (3) using optimal reconstructions of the exchange current obtained by solving Problem P1 (dot-dashed lines) and Problem P2 (dashed lines) as function of the normalized time  $t/t_{tot}$ . Solid lines and dotted line represent the experimental measurements and predictions obtained using the standard Butler-Volmer relation (1) with the nominal parameter values, respectively.

## 5.2 Moderate Discharge Rates

Overall, the results obtained by solving Problems P1 and P2 using the data for moderate discharge rates are qualitatively similar to the results presented in the previous section. In our analysis below, we will therefore focus on highlighting the differences.

Table 4: Material parameters obtained by solving Problem P1.

Charge Rate	Parameter	Value
C/2, discharge	anode reaction rate constant, $k_{0,-}$	$3.165 \times 10^{-12}$
	cathode reaction rate constant, $k_{0,+}$	$1.138 \times 10^{-12}$
	anode anodic transfer coefficient, $\alpha_{a,-}$	0.5001
	cathodic anodic Transfer Coefficient, $\alpha_{c,a}$	0.4999
	electrolyte resistance, $R_{el}$	0.0010
1C, discharge	anode reaction rate constant, $k_{0,-}$	$2.414 \times 10^{-12}$
	cathode reaction rate constant, $k_{0,+}$	$0.867 \times 10^{-12}$
	anode anodic transfer coefficient, $\alpha_{a,-}$	0.5001
	cathodic anodic transfer coefficient, $\alpha_{c,a}$	0.4999
	electrolyte resistance, $R_{el}$	0.0010

The optimal parameters inferred by solving Problem P1 and collected in Table 4 are in the same range as those obtained at low charging rates, cf. Table 3, and also show little variability between the two C-rates considered. The values of the error functional (10) shown in Figure 9 reveal a similar improvement resulting from solving Problem P1 as for the slow discharge rates, cf. Figure 6. However, while in solutions of Problem P2 the reduction of the least-square error  $\mathcal{J}_2$  is still substantial, the errors saturate at the level of  $\mathcal{O}(10^{-2} - 10^{-3})$ .

The optimal form of expression (2b) inferred by solving Problem P1 and shown in Figure 10 is again similar to the nominal form, but has a smaller amplitude, roughly by a factor of 2. On the other hand, the optimal forms of the exchange current  $\hat{i}(c_{s,a})$  inferred by solving Problem P2 reveal significant differences with respect to the corresponding functions obtained at low charging rates, cf. Figure 7. Most importantly, in the present case large values of the exchange current  $\hat{i}(c_{s,a})$  occur at large concentrations close to  $c_{s,a,\max}$ . The data in Figure 11 confirm the small errors evident in Figure 9 are achieved with total potentials closely matching the measurement data. We note that by reducing the value of parameter  $\ell$  in (24) it is in fact possible to obtain overpotentials and total potentials that are indistinguishable (within graphical resolution) from the measured data. However, the price to be paid for that would be increasingly irregular forms of the optimal exchange current  $\hat{i}(c_{s,a})$ .

Finally, we attempt to extract some universal features of the optimal exchange currents determined using measurements acquired at the different charge/discharge rates and, to

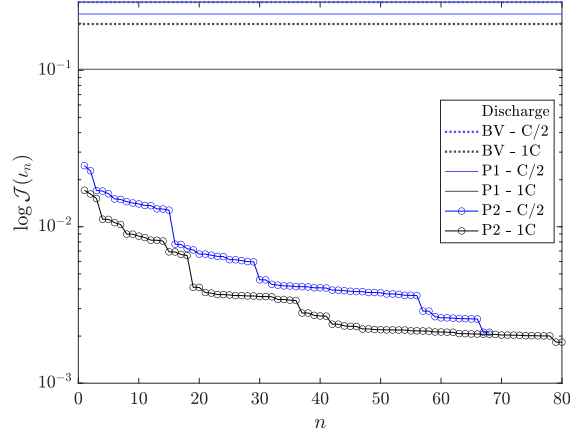


Figure 9: Cost functional  $\mathcal{J}_2$  as function of iterations in the solution of Problem P2 using Algorithm 2 at the C-rate of  $C/2$  (blue lines with circles) and  $1C$  (black lines with circles). The horizontal lines represent the values of the error functional  $\mathcal{J}_1$  corresponding to the standard Butler-Volmer equation (1) (dotted lines) and the terminal values obtained in the solutions of Problem P1 at C-rates of  $C/2$  (blue solid lines) and  $1C$  (black solid lines).

this end, in Figure 12 we compare the optimal reconstructions  $\widehat{i}(c_{s,a})$  obtained by solving Problem P2 for all considered datasets. We see that there is a range of concentrations  $0.25 \times 10^4 \lesssim c_{s,a} \lesssim 2 \times 10^4$  where the inferred exchange currents are qualitatively similar revealing some possibly universal features which include a steep increase of  $\widehat{i}(c_{s,a})$  at lower concentrations  $c_{s,a}$  followed by a gentle and nonmonotonic decrease at higher concentrations. Outside that range the optimal reconstructions  $\widehat{i}(c_{s,a})$  exhibit distinct behaviour specific to each dataset.

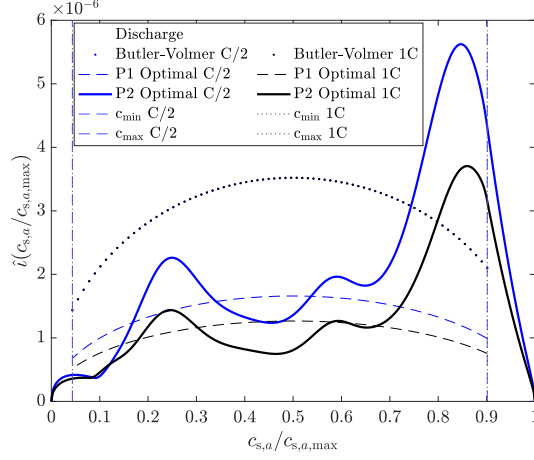


Figure 10: Optimal reconstructions of the exchange current obtained by solving Problem P1 (dashed lines) and Problem P2 (solid lines) as function of the normalized concentration  $c_s/c_{s,\max}$  for the entire concentration range. The standard Butler-Volmer relation (1) with the nominal parameter values is shown using a dotted line whereas the vertical lines represent the bounds of the identifiability intervals at the two C-rates.

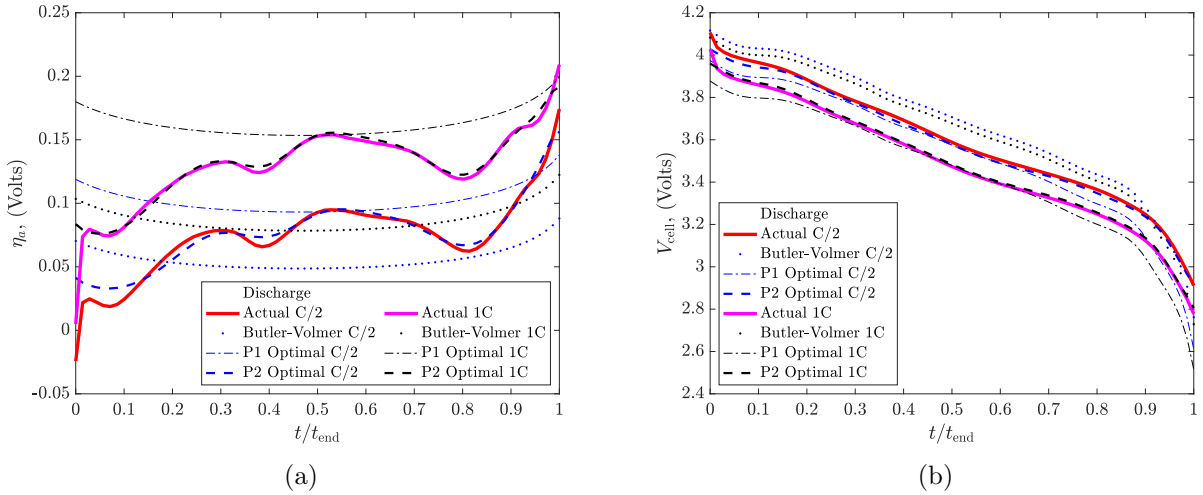


Figure 11: (a) Anode overpotentials and (b) total potentials predicted by the constitutive relation (3) using optimal reconstructions of the exchange current obtained by solving Problem P1 (dot-dashed lines) and Problem P2 (dashed lines) as function of the normalized time  $t/t_{tot}$ . Solid lines and dotted line represent the experimental measurements and predictions obtained using the standard Butler-Volmer relation (1) with the nominal parameter values, respectively.

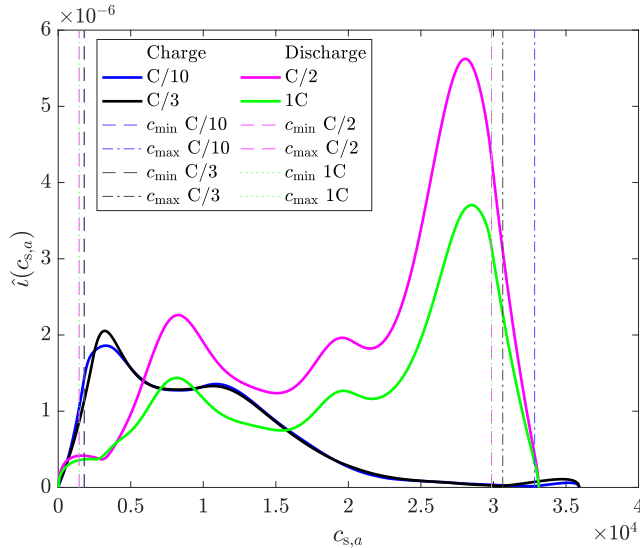


Figure 12: Comparison of optimal reconstructions  $\hat{i}(c_s)$  of the exchange current obtained by solving Problem P2 using all four datasets considered.

## 6 Discussion and Concluding Remarks

In this work, we have developed an inverse modelling approach to infer an optimal form of the concentration-dependent exchange current  $\hat{i}(c_{s,a})$  appearing in a generalization (3) of the Butler-Volmer relation describing intercalation of Li ions into an active material. While many inverse problems have already been solved in the area of electrochemistry,<sup>6,9,10,21–23</sup> this is to the best of our knowledge the first attempt to infer constitutive relations describing an interfacial phenomenon. Although the proposed approach relies on many simplifications, most importantly, on the use of the SPM to describe the transport of Li, it is shown to be computationally robust and thermodynamically consistent. In particular, the model equipped with the inferred optimal exchange currents  $\hat{i}(c_{s,a})$  predicts very accurately the time evolution of the cell voltage which strongly suggests that ansatz (3) and assumptions A1–A3 are physically consistent (we note that such a good match with experimental data need not occur if the model used in the inverse problem does not accurately describe the physics of the problem<sup>9</sup>). Interestingly, by exploiting the coupling between different scales in the model, our approach allows us to reconstruct a constitutive relation defined on the

microscale based on macroscale measurements. The variational formulation of the inverse problem involves averaging of the reconstruction errors over time and concentrations such that the vanishing of the exchange current for small and large concentrations, cf. Assumptions A2 and A3, does not cause problems.

We emphasize that the observations made below are predicated on the accuracy of the material properties which were assumed known in the solution of Problems P1 and P2, cf. Supporting Information (Appendix C). While a significant effort was made to determine these parameters accurately, their inherent uncertainties may have some effect on the obtained results. In particular, one material property known to be difficult to determine with high accuracy is the diffusivity  $D_s(c_s)$  appearing in (4).<sup>55</sup> To probe the effect of its uncertainty, we have solved Problems P1 and P2 in which this diffusivity was allowed to vary over several orders of magnitude. While quantitative details of the reconstructed constitutive relations were different, the key qualitative features of the optimal exchange currents as discussed below were essentially unchanged. That being said, the present study represents only a proof of the concept and more work needs to be done to understand the extent to which our observations about optimal forms of the exchange current could generalize to other battery materials.

The optimal exchange currents  $\widehat{i}(c_{s,a})$  reconstructed by solving Problem P2 based on datasets corresponding to different charging/discharging rates show a qualitatively similar dependence on  $c_{s,a}$  for intermediate concentrations  $0.25 \times 10^4 \lesssim c_{s,a} \lesssim 2 \times 10^4$ , cf. Figure 12. This behaviour is different from the form of the exchange current predicted by the standard Butler-Volmer relation (2b), even after its parameters are calibrated by solving Problem P1. Outside that range, the optimal exchange currents exhibit non-universal features specific to individual cases. In particular, the optimal exchange currents inferred from data representing charging and discharging feature sharp peaks at, respectively, low and high concentrations, cf. Figures 7 and 10, indicating possible hysteresis effects in the constitutive relations. In addition, the results shown in Figure 12 indicate that the exchange current density tends

to be higher during discharging which is consistent with the observations made in earlier studies<sup>56</sup> where this effect was partly attributed to a higher de-solvation energy barrier.

The sharp peaks characterizing the optimal exchange current at low concentrations when charging and at high concentrations when discharging suggest that the electrode kinetics are faster at the beginning of the cycle. This might be due to some interfacial phenomena not accounted for in our model such as, e.g., capacitance effects and variation in the activity coefficient.<sup>57</sup> It is known that the structure of the double layer and ion adsorption can affect electrode kinetics.<sup>26</sup> These phenomena have been implicated in causing anomalies in rate constants and the exchange current, as well as variations in current-potential plots.<sup>26</sup> The behaviour observed at early times in the charge and discharge cycles could be compensating for residual effects produced by the double layer at the electrode interface. In this context, modelling efforts have produced corrections to the Butler-Volmer equation, such as the Frumkin correction which allows the rate constant to be dependent on potential, in order to take into account the effects of the electric double layer and ion adsorption in electrode kinetics.<sup>26</sup> On the other hand, a thermodynamically consistent derivation of the exchange current density shows that its functional form is dependent on the rate constant, concentration, and the activity coefficient.<sup>57</sup> At the same time, the activity of the relevant species is often assumed to be 1, which may not be reflective of the dynamics in the system and could lead to its non-ideal behaviour.<sup>26</sup>

Another possible reason for the presence of large exchange currents at low and high concentrations could be due to the system moving away from equilibrium at the beginning of the cycle protocol when there is a uniform distribution of Li ions in the electrolyte throughout the cell.<sup>13,26</sup> When charging begins, there is a richness of Li near the particle and as the protocol continues, Li moves in the electrolyte towards the anode. The spike observed at early times of the charging protocol could possibly be attributed to the richness of Li near the electrode, which could contribute to a larger exchange current and, consequently, a larger current density at the interface. In the case of a discharge protocol, there is a richness of



Li ions in the anode near the surface and as the cycle continues, Li ions must diffuse from deeper in the electrode to the surface. This is not accounted for in the SPM because the concentration  $c_e$  in the electrolyte is assumed constant, cf. Section 4.1.

The standard formulation of the Butler-Volmer model is based on a simple, single step reaction and as such does not allow for formation of short-lived intermediate products. This is a key assumption which may not be valid in experimental settings; for example, Li-ion batteries often suffer from Li-ion plating, which is a result of fast charging and Li metal plating out onto the surface of the electrode.<sup>58</sup> While this plated material may absorb into the electrode after a certain relaxation time, the side reaction is not captured by the Butler-Volmer kinetic relation<sup>59–61</sup>. Some modelling efforts have attempted to extend the Butler-Volmer to account for such effects.<sup>62–65</sup>

It is also possible that with peaks at low and high Li concentrations the optimal exchange currents  $\tilde{i}(c_{s,a})$  may be compensating for certain effects other than interfacial phenomena which are not accounted for in the model. One such possibility has to do with the nature of Li transport in the active material, which under certain circumstances is known to lead to phase transformations and in turn can significantly affect the diffusivity.<sup>66</sup> The spike in the reconstructed exchange current is located at approximately 12–15% capacity, cf. Figure 7, which could be a result of a rapid increase in the diffusion directly after the phase transition in graphite. When comparing the plots of  $U_{\text{eq}}^a$  and  $\frac{dU_{\text{eq}}^a}{d(c_{s,a}/c_{s,a,\text{max}})}$  vs.  $c_{s,a}/c_{s,a,\text{max}}$  (the latter not shown for brevity), there does appear to be agreement between the minima/maxima observed in the optimal exchange current and the remnants of these phase transitions captured by the equilibrium potential,  $U_{\text{eq}}^a$ . The reconstructed constitutive relations could be therefore compensating for an inadequate transport model used for graphite. It is known that diffusion models are difficult to quantify experimentally and that the physics of transport in the solid is complicated by interfacial phenomena.<sup>9</sup> The literature often reports use of different models of transport in the solid phase based on Fickian diffusion, non-linear diffusion and the Cahn-Hilliard phase separation.<sup>9</sup> However, the anomalous behaviour of optimal exchange currents

at low and high concentrations persisted even when a strongly non-monotonic diffusivities  $D(c_{s,i})$ , similar to the properties measured or inferred for graphite<sup>9,66</sup> were used in the transport equation (4).

More work based on additional datasets is thus needed in order to understand the precise origins of the universal features in the optimal exchange currents  $\widehat{i}(c_{s,i})$  inferred based on different datasets. In particular, it would be beneficial to understand what these universal features can tell us about the validity of the different assumptions used to derive the standard Butler-Volmer relation (1), so that these assumptions could be suitably refined to produce more accurate constitutive models. Even though we have given proof of concept for the approach and its application to interfacial phenomena in electrochemistry, the question of whether it can be used to learn a general improvement to the widely-used “standard” exchange current density in the Butler-Volmer relation (1) remains open. Next steps towards answering this question might include the application of the method using the full DFN framework, thereby generalizing the physics and allowing us to examine higher C-rates. Or, arguably better, one would like to apply this approach to experimental data specifically designed for our purposes, e.g., this might involve a non-porous electrode such that there are fewer device and model parameters, thereby spotlighting the dependence on the interfacial constitutive relation. In the best case, it may then be possible to learn something about the fundamental electrochemistry occurring at material interfaces.

As is evident from the discussion in Section 4.4, a key limiting factor of our approach is its sensitivity to noise. The main issue is that the useful information about the interfacial reaction kinetics is encoded in the overpotential  $\eta$  which at low C-rates represents only a small fraction of the measured cell voltage, cf. Tables 1–2. On the other hand, at higher C-rates where this proportion increases, the SPM loses its validity. A preferred solution would thus be to formulate the inverse problem based on the full DFN model (or one of its reductions, but more complete than the SPM), as this would make it possible to use data obtained at higher C-rates where the overpotential  $\eta$  represents a larger proportion of the measured voltage.

Such an inverse problem will be mathematically more complicated since, unlike the case of the SPM, the solutions of the DFN model depend on the form of the constitutive relation describing ion intercalation. Another limitation of the proposed approach is that the optimal forms of the constitutive relation depend on the C-rate, cf. Figures 10 and 12. While this is not uncommon when an inverse problem is solved using multiple experimental datasets, this complicates application of the method in practice when one needs to model battery cells at different C-rates. A possible solution is to infer an “average” optimal exchange current by simultaneously fitting voltage curves corresponding to several C-rates. When extending the proposed analysis to alternative materials, considerations such as multiphase intercalation<sup>67,68</sup> and mixed conduction effects<sup>44</sup> would need to be taken into account. The former would necessitate redefining diffusivity in the bulk whereas the latter would require simultaneous solution of the diffusion and conduction problems at the particle level. We plan to pursue such extensions of the present approach in the near future.

In principle, the framework developed in the present investigation could be used to study other interfacial phenomena, where experimental data can be leveraged to learn the optimal forms of the relevant constitutive relations. Some interesting problems of this type include the reconstruction of constitutive relations governing the Hodgkin-Huxley dynamics of ion transfer through a cell membrane,<sup>17</sup> the Shockley-Read-Hall recombination of electrons in a semiconductor,<sup>69,70</sup> or the charge density of an adsorbed layer formed between a charged interface and an electrolyte.<sup>71</sup>

## Acknowledgement

LD, KJS, GRG and BP were supported by a Collaborative Research & Development grant # CRD494074-16 from Natural Sciences & Engineering Research Council of Canada. JF and SS were supported by the Faraday Institution, UK (grant number FIRG003).

# A Limiting Behaviour of Constitutive Relationships at Small and Large Concentrations

We derive conditions that must be satisfied by the function  $\iota(c_s)$  for  $c_s \rightarrow 0, c_{s,max}$  in order for the constitutive relation (3) to be physically consistent. We note that  $c_s = \iota^{-1}(\Delta\phi)$  relates the potential  $\Delta\phi$  to the concentration  $c_s$  and the range of  $\iota^{-1}(\Delta\phi)$  is  $0 \leq \iota^{-1}(\Delta\phi) \leq c_{s,max}$ . The equilibrium potential can be separated into a bounded portion  $u_{eq}$  and an unbounded part given by<sup>28</sup>

$$U_{eq}^i(\Delta\phi) = \frac{RT}{F(\alpha_a + \alpha_c)} \log \left( \frac{k_c c_e (c_{s,max} - \iota^{-1}(\Delta\phi))}{k_a \iota^{-1}(\Delta\phi)} \right) + u_{eq}. \quad (15)$$

Plugging this expression into (2), we obtain

$$j = F\iota(c_s) \left[ e^{\frac{\alpha_a F}{RT}(\Delta\phi - u_{eq})} \left( \frac{k_c c_e (c_{s,max} - c_s)}{k_a c_s} \right)^{-\frac{\alpha_a}{\alpha_a + \alpha_c}} - e^{\frac{\alpha_c F}{RT}(\Delta\phi - u_{eq})} \left( \frac{k_c c_e (c_{s,max} - c_s)}{k_a c_s} \right)^{\frac{\alpha_c}{\alpha_a + \alpha_c}} \right], \quad (16)$$

which should vanish when  $c_s \rightarrow 0$  as the electrode cannot be depleted at vanishing concentrations, and when  $c_s \rightarrow c_{s,max}$  as the electrode cannot continue to be filled once the maximum concentration is reached. In order to overcome the divergence of the factors in the parentheses in these limits, we must require the function  $\iota(c_s)$  to vanish sufficiently rapidly as  $c_s \rightarrow 0, c_{s,max}$ . More specifically, expression (16) will vanish in these limits provided

$$\iota(c_s) = \begin{cases} \mathcal{O} \left[ \left( \frac{k_a c_s}{k_c c_e (c_{s,max} - c_s)} \right)^\omega \right], & \omega > \frac{\alpha_c}{\alpha_a + \alpha_c}, \quad \text{as } c_s \rightarrow 0, \\ \mathcal{O} \left[ \left( \frac{k_c c_e (c_{s,max} - c_s)}{k_a c_s} \right)^\gamma \right], & \gamma > \frac{\alpha_a}{\alpha_a + \alpha_c}, \quad \text{as } c_s \rightarrow c_{s,max} \end{cases}. \quad (17)$$

Condition (17) must be incorporated into the formulation of Problem P2.

## B Computation of Gradients

We begin by computing the Gâteaux (directional) derivative of the error functional (11) defined as  $\mathcal{J}'_2(\iota(c_s); \iota'(c_s)) = \lim_{\epsilon \rightarrow 0} \epsilon^{-1} [\mathcal{J}_2(\iota(c_s) + \epsilon \iota'(c_s)) - \mathcal{J}_2(\iota(c_s))]$ , where  $\iota'(c_s)$  is an arbitrary perturbation of  $\iota(c_s)$ , and obtain

$$\mathcal{J}'_2(\iota(c_s); \iota'(c_s)) = \int_0^{t_f} \eta'(\iota(c_s(t)); \iota'(c_s)) [\eta(\iota(c_s(t))) - \bar{\eta}(\iota(c_s(t)))] dt. \quad (18)$$

The Riesz representation theorem then asserts that the Gâteaux differential (18) can be expressed as

$$\mathcal{J}'_2(\iota(c_s); \iota'(c_s)) = \left\langle \nabla^{L^2} \mathcal{J}, \iota' \right\rangle_{L^2} = \int_0^{c_{s,max}} \nabla^{L^2} \mathcal{J}_2(c_s) \cdot \iota'(c_s) dc, \quad (19)$$

where  $\nabla^{L^2} \mathcal{J}_2(c_s)$  is the gradient of the error functional computed with respect to the  $L^2$  inner product  $\langle \cdot, \cdot \rangle_{L^2}$ . To transform (18) into a form consistent with (19), where  $\iota'(c_s)$  appears as a factor and integration is performed with respect to  $c_s$ , we define  $\iota_\epsilon(c_s) = \iota(c_s) + \epsilon \iota'(c_s) + \mathcal{O}(\epsilon^2)$  so that the perturbed Butler-Volmer relation is  $j_\epsilon = \iota(c_s) \psi(\Delta\phi, c_s) + \epsilon \iota'(c_s) \psi(\Delta\phi, c_s) + \mathcal{O}(\epsilon^2)$ . Then, the corresponding cell overpotential,  $\eta$ , is

$$\begin{aligned} \eta &= \psi^{-1} \left( \frac{I}{AF [\iota(c_s) + \epsilon \iota'(c_s) + \mathcal{O}(\epsilon^2)]} \right) \\ &= \psi^{-1} \left( \frac{I}{AF \iota(c_s)} \right) + \underbrace{\epsilon \left( \left[ \psi^{-1} \left( \frac{I}{AF \iota(c_s)} \right) \right]' \frac{-I}{(AF)(\iota(c_s))^2} \right)}_{\eta'(\iota(c_s(t)); \iota'(c_s))} \iota'(c_s) + \mathcal{O}(\epsilon^2). \end{aligned} \quad (20)$$

Using (20) in (18), we obtain

$$\begin{aligned} \mathcal{J}'_2(\iota(c_s); \iota'(c_s)) &= \int_0^{t_f} \frac{-I\iota'(c_s(t))}{(AF)(\iota(c_s(t)))^2} [\eta(\iota(c_s(t))) - \bar{\eta}(\iota(c_s(t)))] dt \\ &= \int_0^{c_{s,max}} \frac{1}{\psi' \left( \frac{I}{AF\iota(c_s)} \right)} \frac{-I\iota'(c_s)}{(AF)(\iota(c_s))^2} (\eta(\iota(c_s)) - \bar{\eta}(\iota(c_s))) \left| \frac{dt}{dc_s} \right| dc_s, \end{aligned} \quad (21)$$

where the integration variable has been changed from  $t$  to  $c_s$  using the relation  $c_s = c_s(t)$  defined by the numerical solution of the SPM. We note that (21) is now in a form consistent with the Riesz representation (19), which allows us to define the  $L^2$  gradient as

$$\nabla^{L^2} \mathcal{J}_2 = \left( \frac{1}{\psi' \left( \frac{I}{AF\iota(c_s)} \right)} \frac{-I}{(AF)(\iota(c_s))^2} \right) (\eta(\iota(c_s)) - \bar{\eta}(\iota(c_s))) \left| \frac{dt}{dc_s} \right|, \quad c_s \in [0, c_{s,max}]. \quad (22)$$

We observe that while expression (22) is defined for  $c_s \in [0, c_{s,max}]$ , it will be nonzero only for  $c_s \in [c_<, c_>] = \mathcal{I}$ , where  $c_< = \inf_{t \in [0, t_f]} c_s(t)$ ,  $c_> = \sup_{t \in [0, t_f]} c_s(t)$  and  $\mathcal{I}$  is referred to as the *identifiability interval*. In other words, the sensitivity information can be obtained only for concentration values in the identifiability interval, which is the range of concentrations attained in a given experiment. In addition, expression (22) can produce discontinuous functions of  $c_s$  which, when used in (12), would not produce constitutive relations with the required regularity, cf. Assumption A1 in Section 2. In the light of expression (12), the regularity of the optimal constitutive relation  $\tilde{\iota}(c_s)$  is determined by the smoothness of the gradients  $\nabla \mathcal{J}_2(c_s)$ .

Gradients with the required regularity are constructed using the Riesz identity (19) extended to the Sobolev space  $H^1([0, c_{s,max}])$  of functions with square-integrable distributional derivatives, namely,

$$\mathcal{J}'_2(\iota(c_s); \iota'(c_s)) = \left\langle \nabla^{L^2} \mathcal{J}_2, \iota' \right\rangle_{L^2} = \left\langle \nabla \mathcal{J}_2, \iota' \right\rangle_{H^1}, \quad (23)$$

which makes it possible to identify the Gâteaux differential (21) with the  $H^1$  inner product defined as

$$\langle \nabla \mathcal{J}_2, \iota' \rangle_{H^1} = \int_0^{c_{s,max}} \left[ \nabla \mathcal{J}_2 \iota' + \ell^2 \frac{d(\nabla \mathcal{J}_2)}{dc_s} \frac{d\iota'}{dc_s} \right] dc_s, \quad (24)$$

where  $\ell \in \mathbb{R}$  is a parameter with the meaning of a characteristic concentration. We note that as long as  $0 < \ell < \infty$ , inner products (24) with different values of  $\ell$  are equivalent in the sense of norm equivalence. However, the choice of the value of parameter  $\ell$  is important in computations as it controls the degree of regularization in the solution of Problem P2. Performing integration by parts with respect to  $c_s$  on the second term in (24), we obtain

$$\langle \nabla \mathcal{J}_2, \iota' \rangle_{H^1} = \int_0^{c_{s,max}} \left( Id - \ell^2 \frac{d^2}{dc_s^2} \right) \nabla \mathcal{J}_2 \iota' dc_s - \ell^2 \frac{d(\nabla \mathcal{J}_2)}{dc_s} \iota' \Big|_0^{c_{s,max}}. \quad (25)$$

Noting that the perturbation of the exchange current  $\iota'(c_s)$  (i.e., the “test” function) is arbitrary and the Sobolev gradient  $\nabla \mathcal{J}_2(c_s)$  needs to vanish at the endpoints, such that  $\iota'(0) = \iota'(c_{s,max}) = 0$  (cf. Assumptions A2–A3 in Section 2 and Appendix A), relation (25) implies

$$\left( Id - \ell^2 \frac{d^2}{dc_s^2} \right) \nabla \mathcal{J}_2 = \nabla^{L^2} \mathcal{J}_2 \quad \text{for } c_s \in (0, c_{s,max}), \quad (26a)$$

$$\nabla \mathcal{J}_2 = 0 \quad \text{at } c_s = 0, c_{s,max}, \quad (26b)$$

which shows that the Sobolev gradient can be obtained by solving a boundary-value problem with the  $L^2$  gradient (22) appearing as a source term. We add that this formalism allows us to propagate the sensitivity information outside the identifiability interval  $\mathcal{I}$  such that the Sobolev gradient  $\nabla \mathcal{J}_2(c_s)$  is a continuous functions not identically equal to zero for  $c_s \in [0, c_{s,max}] \setminus \mathcal{I}$ . It is known<sup>72</sup> that extraction of gradients in spaces of smoother functions such as  $H^1$  can be interpreted as low-pass filtering of the  $L^2$  gradients with parameter  $\ell$

acting as the cut-off length-scale of the filter. The value of  $\ell$  can significantly affect the rate of convergence of the iterative procedure (12).

## C Experimental Parameters

### C.1 Slow charge rates

Table 5: Electrode specific experimental parameters for slow charge rate experiments.<sup>29</sup>

Parameter	Units	Anode	Cathode
electrode thickness, $L$ ,	$\mu\text{m}$	50	50
electrode particle radius, $R_p$	$\mu\text{m}$	9	6.5
electrode cross-section area, $A$	$\text{m}^2$	0.000551	0.000551
volume fraction of electrolyte, $\epsilon_l$	unitless	0.1	0.1
Brunauer-Emmett-Teller surface area, $b_0$	$\text{m}^{-1}$	$3.0 \times 10^5$	$4.1538 \times 10^5$
conductivity in solid, $\sigma_0$	$\text{Sm}^{-1}$	14	68.1
permeability factor of electrode, $\mathcal{B}_0$	unitless	0.0493	0.0515
reaction rate constant, $k_0$	$\text{m}^{5/2}\text{s}^{-1}\text{mol}^{-1/2}$	$1.8742 \times 10^{-10}$	$4.9375 \times 10^{-11}$
maximum concentration of Lithium in solid, $c_{s,max}$	$\text{mol m}^{-3}$	35920	42580
initial concentration of Lithium in electrode, $c_0$	$\text{mol m}^{-3}$	1000	1000
activation energy, $E_i$	$\text{J mol}^{-1}$	30300	80600

Table 6: Global experimental parameters for slow charge rate experiments.<sup>29</sup>

Parameter	Units	Value
temperature, $T$	K	295.15
relative temperature, $\hat{T}$	K	296
universal gas constant, $R$	$\text{J mol}^{-1} \text{K}^{-1}$	8.3144
C/10 current, $I_0$	A	$2.29 \times 10^{-3}$
C/3 current, $I_0$	A	0.0076
transference number, $t^+$	unitless	0.26

Diffusivities in the electrodes are assumed to depend on Arrhenius temperature and are given



by

$$D_s(c_{s,i}, T) = D_s(c_{s,i})e^{\left(\frac{E_i}{RT} - \frac{E_i}{RT}\right)},$$

$$D_s(c_{s,a}) = 8.4 \times 10^{-9} e^{-11.3\left(\frac{c_{s,a}}{c_{s,a,max}}\right)} + 8.2 \times 10^{-12},$$

$$D_s(c_{s,c}) = 3.7 \times 10^{-13} - 3.4 \times 10^{-13} e^{-12\left(\frac{c_{s,c}}{c_{s,c,max}} - 0.62\right)}$$

with units of  $\text{m}^2/\text{s}$ .

## C.2 Moderate discharge rates

Table 7: Electrode specific experimental parameters for moderate discharge rate experiments.<sup>30</sup>

Parameter	Units	Anode	Cathode
electrode thickness, $L$ ,	$\mu\text{m}$	85.2	75.6
electrode particle radius, $R_p$	$\mu\text{m}$	5.86	5.22
electrode cross-section area, $A$	$\text{m}^2$	0.10465	0.1027
volume fraction of electrolyte, $\epsilon_l$	unitless	0.25	0.335
Brunauer-Emmett-Teller surface area, $b_0$	$\text{m}^{-1}$	$3.8396 \times 10^5$	$3.8218 \times 10^5$
conductivity in solid, $\sigma_0$	$\text{Sm}^{-1}$	215	0.18
permeability factor of electrode, $\mathcal{B}_0$	unitless	0.0177	0.0701
reaction rate Constant, $k_0$	$\text{m}^{5/2}\text{s}^{-1}\text{mol}^{-1/2}$	$0.0672 \times 10^{-10}$	$0.3545 \times 10^{-10}$
maximum concentration of Lithium in solid, $c_{s,max}$	$\text{mol m}^{-3}$	33133	63104
initial concentration of Lithium in electrode, $c_0$	$\text{mol m}^{-3}$	1000	1000

Table 8: Global experimental parameters for moderate discharge rate experiments.<sup>30</sup>

Parameter	Units	Value
temperature, $T$	K	298.15
C/2 current, $I_0$	A	2.5
1C current, $I_0$	A	5
Transference Number, $t^+$	unitless	0.259

Transport in the electrodes is assumed to be governed by Fickian diffusion with

$$D_s(c_{s,a}) = 3.3 \times 10^{-10},$$

$$D_s(c_{s,c}) = 4 \times 10^{-11}$$

and with units of  $\text{m}^2/\text{s}$ .

## D Checklist To Report Theoretical Battery Studies

Here, we complete the checklist for the minimal information set.<sup>73</sup>

1. *Have you provided all assumptions, theory, governing equations, initial and boundary conditions, material properties (e.g., open-circuit potential) with appropriate precision and literature sources, constant states (e.g., temperature), etc.?*

Remarks: Yes, all elements of the model have been stated in the main text and the supplemental information.

2. *If the calculations have a probabilistic component (e.g., Monte Carlo, initial configuration in Molecular Dynamics, etc.), did you provide statistics (mean, standard deviation, confidence interval, etc.) from multiple ( $\geq 3$ ) runs of a representative case?*

Remarks: Yes, Monte Carlo simulations were run with 3000 samples. The methodology is reported in the main text and confidence intervals are included on the relevant figures.

3. *If data-driven calculations are performed (e.g., machine learning), did you specify dataset origin, the rationale behind choosing it, what information it contains, and the specific portion of it being utilized? Have you described the thought process for choosing a specific modeling paradigm?*

Remarks: While the methodology used is data driven, it relies on calculus of variations rather than machine learning. The experimental data is described in Section 3 whereas the optimization scheme is outlined in Algorithms 1 and 2.

4. *Have you discussed all sources of potential uncertainty, variability, and errors in the modeling results and their impact on quantitative results and qualitative trends? Have*

*you discussed the sensitivity of modeling (and numerical) inputs such as material properties, time step, domain size, neural network architecture, etc. where they are variable or uncertain?*

Remarks: Yes, this discussion is provided in Sections 4.4 and 6 in the main text.

5. *Have you sufficiently discussed new or not widely familiar terminology and descriptors for clarity? Did you use these terms in their appropriate context to avoid misinterpretation? Enumerate these terms in the “Remarks”.*

Remarks: Yes, the terminology is consistent with the conventions used in the research fields.

## References

- (1) Wang, A.; O’Kane, S. E.; Planella, F. B.; Le Houx, J.; O’Regan, K.; Zyskin, M.; Edge, J. S.; Monroe, C.; Cooper, S.; Howey, D. A. et al. Review of parameterisation and a novel database (LiionDB) for continuum Li-ion battery models. *Progress in Energy* **2022**, *4*, 032004.
- (2) Lv, C.; Zhou, X.; Zhong, L.; Yan, C.; Srinivasan, M.; Seh, Z. W.; Liu, C.; Pan, H.; Li, S.; Wen, Y. et al. Machine learning: an advanced platform for materials development and state prediction in lithium-ion batteries. *Advanced Materials* **2022**, *34*, 2101474.
- (3) Houchins, G.; Viswanathan, V. An accurate machine-learning calculator for optimization of Li-ion battery cathodes. *The Journal of Chemical Physics* **2020**, *153*, 054124.
- (4) Chemali, E.; Kollmeyer, P. J.; Preindl, M.; Emadi, A. State-of-charge estimation of Li-ion batteries using deep neural networks: A machine learning approach. *Journal of Power Sources* **2018**, *400*, 242–255.
- (5) Klett, M.; Giesecke, M.; Nyman, A.; Hallberg, F.; Lindström, R. W.; Lindbergh, G.;

- Furo, I. Quantifying Mass Transport during Polarization in a Li Ion Battery Electrolyte by in Situ Li NMR Imaging. *J. Am. Chem. Soc.* **2012**, *134*, 14654–14657.
- (6) Sethurajan, A. K.; Krachkovskiy, S. A.; Halalay, I. C.; Goward, G. R.; Protas, B. Accurate characterization of ion transport properties in binary symmetric electrolytes using in situ NMR imaging and inverse modeling. *The Journal of Physical Chemistry B* **2015**, *119*, 12238–12248.
- (7) Richardson, G.; Foster, J. M.; Sethurajan, A. K.; Krachkovskiy, S. A.; Halalay, I. C.; Goward, G. R.; Protas, B. The effect of ionic aggregates on the transport of charged species in lithium electrolyte solutions. *Journal of The Electrochemical Society* **2018**, *165*, H561–H567.
- (8) Sethurajan, A. K.; Foster, J. M.; Richardson, G.; Krachkovskiy, S. A.; Bazak, J. D.; Goward, G. R.; Protas, B. Incorporating Dendrite Growth into Continuum Models of Electrolytes: Insights from NMR Measurements and Inverse Modeling. *Journal of The Electrochemical Society* **2019**, *166*, A1591–A1602.
- (9) Escalante, J. M.; Ko, W.; Foster, J. M.; Krachkovskiy, S.; Goward, G.; Protas, B. Discerning models of phase transformations in porous graphite electrodes: Insights from inverse modelling based on MRI measurements. *Electrochimica Acta* **2020**, *349*, 136290.
- (10) Escalante, J. M.; Sahu, S.; Foster, J. M.; Protas, B. On Uncertainty Quantification in the Parametrization of Newman-type Models of Lithium-ion Batteries. *Journal of The Electrochemical Society* **2021**, *168*, 110519.
- (11) Chen, W.; Liang, J.; Yang, Z.; Li, G. A review of lithium-ion battery for electric vehicle applications and beyond. *Energy Procedia* **2019**, *158*, 4363–4368.
- (12) Blomgren, G. E. The development and future of lithium ion batteries. *Journal of The Electrochemical Society* **2016**, *164*, A5019.

- (13) Newman, J.; Thomas-Alyea, K. E. *Electrochemical Systems*; John Wiley and Sons, 2004.
- (14) Hamelers, H. V.; Ter Heijne, A.; Stein, N.; Rozendal, R. A.; Buisman, C. J. Butler–Volmer–Monod model for describing bio-anode polarization curves. *Bioresource technology* **2011**, *102*, 381–387.
- (15) Compton, R. G.; Banks, C. E. *Understanding voltammetry, 2nd ed.*; Imperial College Press London, 2011.
- (16) Oyarzun, D. I.; Zhan, C.; Hawks, S. A.; Cerón, M. R.; Kuo, H. A.; Loeb, C. K.; Aydin, F.; Pham, T. A.; Stadermann, M.; Campbell, P. G. Unraveling the Ion Adsorption Kinetics in Microporous Carbon Electrodes: A Multiscale Quantum-Continuum Simulation and Experimental Approach. *ACS Applied Materials & Interfaces* **2021**, *13*, 23567–23574.
- (17) Hodgkin, A. L.; Huxley, A. F. A quantitative description of membrane current and its application to conduction and excitation in nerve. *The Journal of physiology* **1952**, *117*, 500.
- (18) Banks, H. T.; Kunisch, K. *Estimation techniques for distributed parameter systems*; Springer Science & Business Media, 2012.
- (19) Tarantola, A. *Inverse Problem Theory and Methods for Model Parameter Estimation*; Society for Industrial and Applied Mathematics, 2005.
- (20) Isakov, V. *Inverse Problems for Partial Differential Equations*; Applied Mathematical Sciences 127; Springer, 1998.
- (21) Bukshytynov, V.; Volkov, O.; Protas, B. On Optimal Reconstruction of Constitutive Relations. *Physica D: Nonlinear Phenomena* **2011**, *240*, 1228–1244.

- (22) Sethurajan, A.; Krachkovskiy, S.; Goward, G.; Protas, B. Bayesian uncertainty quantification in inverse modeling of electrochemical systems. *Journal of Computational Chemistry* **2019**, *40*, 740–752.
- (23) Bukshtynov, V.; Protas, B. Optimal reconstruction of material properties in complex multiphysics phenomena. *Journal of Computational Physics* **2013**, *242*, 889 – 914.
- (24) Dickinson, E. J.; Wain, A. J. The Butler-Volmer equation in electrochemical theory: Origins, value, and practical application. *Journal of Electroanalytical Chemistry* **2020**, *872*, 114145.
- (25) Latz, A.; Zausch, J. Thermodynamic derivation of a Butler–Volmer model for intercalation in Li-ion batteries. *Electrochimica Acta* **2013**, *110*, 358–362.
- (26) Bard, A. J.; Faulkner, L. R. *Electrochemical methods: Fundamentals and applications*; Wiley New York, 2001.
- (27) Fletcher, S. Tafel slopes from first principles. *Journal of Solid State Electrochemistry* **2009**, *13*, 537–549.
- (28) Richardson, G. W.; Foster, J. M.; Ranom, R.; Please, C. P.; Ramos, A. M. Charge transport modelling of Lithium-ion batteries. *European Journal of Applied Mathematics* **2020**, 1–49.
- (29) Sanders, K. J.; Aguilera, A. R.; Keffer, J. R.; Balcom, B. J.; Halalay, I. C.; Goward, G. R. Transient lithium metal plating on graphite: Operando  $^7\text{Li}$  nuclear magnetic resonance investigation of a battery cell using a novel RF probe. *Carbon* **2022**, 377–385.
- (30) Chen, C.-H.; Planella, F. B.; O’regan, K.; Gastol, D.; Widanage, W. D.; Kendrick, E. Development of experimental techniques for parameterization of multi-scale lithium-ion battery models. *Journal of The Electrochemical Society* **2020**, *167*, 080534.

- (31) Richardson, G.; Korotkin, I.; Ranom, R.; Castle, M.; Foster, J. Generalised single particle models for high-rate operation of graded lithium-ion electrodes: systematic derivation and validation. *Electrochimica Acta* **2020**, *339*, 135862.
- (32) Korotkin, I.; Sahu, S.; O’Kane, S. E.; Richardson, G.; Foster, J. M. Dandelion v1: An extremely fast solver for the Newman model of lithium-ion battery (dis) charge. *Journal of The Electrochemical Society* **2021**, *168*, 060544.
- (33) Wu, S.-L.; Zhang, W.; Song, X.; Shukla, A. K.; Liu, G.; Battaglia, V.; Srinivasan, V. High rate capability of Li (Ni<sub>1/3</sub>Mn<sub>1/3</sub>Co<sub>1/3</sub>) O<sub>2</sub> electrode for Li-ion batteries. *Journal of The Electrochemical Society* **2012**, *159*, A438.
- (34) Nguyen, T.-T.; Delobel, B.; Berthe, M.; Fleutot, B.; Demortière, A.; Delacourt, C. Mathematical Modeling of Energy-Dense NMC Electrodes: I. Determination of Input Parameters. *Journal of The Electrochemical Society* **2022**, *169*, 040546.
- (35) Doyle, M.; Fuller, T. F.; Newman, J. Modeling of Galvanostatic Charge and Discharge of the Lithium/Polymer/Insertion Cell. *Journal of The Electrochemical Society* **1993**, *140*, 1526–1533.
- (36) Fuller, T. F.; Doyle, M.; Newman, J. Simulation and optimization of the dual lithium ion insertion cell. *Journal of the Electrochemical Society* **1994**, *141*, 1.
- (37) Mistry, A. N.; Smith, K.; Mukherjee, P. P. Secondary-phase stochastics in lithium-ion battery electrodes. *ACS applied materials & interfaces* **2018**, *10*, 6317–6326.
- (38) Mistry, A.; Trask, S.; Dunlop, A.; Jeka, G.; Polzin, B.; Mukherjee, P. P.; Srinivasan, V. Quantifying negative effects of carbon-binder networks from electrochemical performance of porous li-ion electrodes. *Journal of The Electrochemical Society* **2021**, *168*, 070536.

- (39) Mistry, A.; Usseglio-Viretta, F. L.; Colclasure, A.; Smith, K.; Mukherjee, P. P. Fingerprinting redox heterogeneity in electrodes during extreme fast charging. *Journal of The Electrochemical Society* **2020**, *167*, 090542.
- (40) Hein, S.; Danner, T.; Westhoff, D.; Prifling, B.; Scurtu, R.; Kremer, L.; Hoffmann, A.; Hilger, A.; Osenberg, M.; Manke, I. et al. Influence of conductive additives and binder on the impedance of lithium-ion battery electrodes: effect of morphology. *Journal of The Electrochemical Society* **2020**, *167*, 013546.
- (41) Ferraro, M. E.; Trembacki, B. L.; Brunini, V. E.; Noble, D. R.; Roberts, S. A. Electrode mesoscale as a collection of particles: coupled electrochemical and mechanical analysis of NMC cathodes. *Journal of The Electrochemical Society* **2020**, *167*, 013543.
- (42) Mistry, A.; Heenan, T.; Smith, K.; Shearing, P.; Mukherjee, P. P. Asphericity can cause nonuniform lithium intercalation in battery active particles. *ACS Energy Letters* **2022**, *7*, 1871–1879.
- (43) Verbrugge, M. W.; Koch, B. J. Modeling lithium intercalation of single-fiber carbon microelectrodes. *Journal of the Electrochemical Society* **1996**, *143*, 600.
- (44) Johnson, I. D.; Mistry, A. N.; Yin, L.; Murphy, M.; Wolfman, M.; Fister, T. T.; Lapidus, S. H.; Cabana, J.; Srinivasan, V.; Ingram, B. J. Unconventional Charge Transport in MgCr<sub>2</sub>O<sub>4</sub> and Implications for Battery Intercalation Hosts. *Journal of the American Chemical Society* **2022**, *144*, 14121–14131.
- (45) Amin, R.; Ravnsbæk, D. B.; Chiang, Y.-M. Characterization of electronic and ionic transport in Li<sub>1-x</sub>Ni<sub>0.8</sub>Co<sub>0.15</sub>Al<sub>0.05</sub>O<sub>2</sub> (NCA). *Journal of the electrochemical society* **2015**, *162*, A1163.
- (46) Amin, R.; Chiang, Y.-M. Characterization of electronic and ionic transport in Li<sub>1-x</sub>Ni<sub>0.33</sub>Mn<sub>0.33</sub>Co<sub>0.33</sub>O<sub>2</sub> (NMC333) and Li<sub>1-x</sub>Ni<sub>0.50</sub>Mn<sub>0.20</sub>Co<sub>0.30</sub>O<sub>2</sub> (NMC523) as a function of Li content. *Journal of The Electrochemical Society* **2016**, *163*, A1512.



- (47) Amin, R.; Maier, J.; Balaya, P.; Chen, D.; Lin, C. Ionic and electronic transport in single crystalline LiFePO<sub>4</sub> grown by optical floating zone technique. *Solid State Ionics* **2008**, *179*, 1683–1687.
- (48) Santhanagopalan, S.; Guo, Q.; Ramadass, P.; White, R. E. Review of models for predicting the cycling performance of lithium ion batteries. *Journal of power sources* **2006**, *156*, 620–628.
- (49) Schmalstieg, J.; Rahe, C.; Ecker, M.; Sauer, D. U. Full cell parameterization of a high-power lithium-ion battery for a physico-chemical model: Part I. Physical and electrochemical parameters. *Journal of The Electrochemical Society* **2018**, *165*, A3799.
- (50) Marquis, S. G.; Sulzer, V.; Timms, R.; Please, C. P.; Chapman, S. J. An asymptotic derivation of a single particle model with electrolyte. *Journal of The Electrochemical Society* **2019**, *166*, A3693.
- (51) Adams, R. A.; Fournier, J. F. *Sobolev Spaces*; Elsevier, 2005.
- (52) Press, W. H.; Flanner, B. P.; Teukolsky, S. A.; Vetterling, W. T. *Numerical Recipes: the Art of Scientific Computations*; Cambridge University Press, 1986.
- (53) Devore, J. L. *Probability and Statistics for Engineering and the Sciences*; Cengage learning, 2011.
- (54) Ecker, M.; Tran, T. K. D.; Dechent, P.; Käbitz, S.; Warnecke, A.; Sauer, D. U. Parameterization of a Physico-Chemical Model of a Lithium-Ion Battery: I. Determination of Parameters. *Journal of The Electrochemical Society* **2015**, *162*, A1836–A1848.
- (55) Park, M.; Zhang, X.; Chung, M.; Less, G. B.; Sastry, A. M. A review of conduction phenomena in Li-ion batteries. *Journal of Power Sources* **2010**, *195*, 7904–7929.
- (56) Jow, T. R.; Delp, S. A.; Allen, J. L.; Jones, J.-P.; Smart, M. C. Factors limiting Li+

- charge transfer kinetics in Li-ion batteries. *Journal of the electrochemical society* **2018**, *165*, A361.
- (57) Christensen, J.; Newman, J. Stress generation and fracture in lithium insertion materials. *Journal of Solid State Electrochemistry* **2006**, *10*, 293–319.
- (58) O’Kane, S. E.; Ai, W.; Madabattula, G.; Alonso-Alvarez, D.; Timms, R.; Sulzer, V.; Edge, J. S.; Wu, B.; Offer, G. J.; Marinescu, M. Lithium-ion battery degradation: how to model it. *Physical Chemistry Chemical Physics* **2022**, *24*, 7909–7922.
- (59) Zinth, V.; Von Lüders, C.; Hofmann, M.; Hattendorff, J.; Buchberger, I.; Erhard, S.; Rebelo-Kornmeier, J.; Jossen, A.; Gilles, R. Lithium plating in lithium-ion batteries at sub-ambient temperatures investigated by in situ neutron diffraction. *Journal of Power Sources* **2014**, *271*, 152–159.
- (60) Uhlmann, C.; Illig, J.; Ender, M.; Schuster, R.; Ivers-Tiffée, E. In situ detection of lithium metal plating on graphite in experimental cells. *Journal of Power Sources* **2015**, *279*, 428–438.
- (61) Wandt, J.; Jakes, P.; Granwehr, J.; Eichel, R.-A.; Gasteiger, H. A. Quantitative and time-resolved detection of lithium plating on graphite anodes in lithium ion batteries. *Materials Today* **2018**, *21*, 231–240.
- (62) Yang, X.-G.; Leng, Y.; Zhang, G.; Ge, S.; Wang, C.-Y. Modeling of lithium plating induced aging of lithium-ion batteries: Transition from linear to nonlinear aging. *Journal of Power Sources* **2017**, *360*, 28–40.
- (63) Yang, X.-G.; Ge, S.; Liu, T.; Leng, Y.; Wang, C.-Y. A look into the voltage plateau signal for detection and quantification of lithium plating in lithium-ion cells. *Journal of Power Sources* **2018**, *395*, 251–261.

- (64) O’Kane, S. E.; Campbell, I. D.; Marzook, M. W.; Offer, G. J.; Marinescu, M. Physical origin of the differential voltage minimum associated with lithium plating in Li-ion batteries. *Journal of The Electrochemical Society* **2020**, *167*, 090540.
- (65) Sahu, S.; Foster, J. M. A continuum model for lithium plating and dendrite formation in lithium-ion batteries: Formulation and validation against experiment. *Journal of Energy Storage* **2023**, *60*, 106516.
- (66) Levi, M.; Wang, C.; Markevich, E.; Aurbach, D.; Chvoj, Z. Noteworthy electroanalytical features of the stage 4 to stage 3 phase transition in lithiated graphite. *Journal of Solid State Electrochemistry* **2003**, *8*, 40–43.
- (67) Verbrugge, M. W.; Baker, D. R.; Chen, S.; He, M.; Cai, M. Cation Mixing and Capacity Loss in Li—Ni<sub>0.6</sub>Mn<sub>0.2</sub>Co<sub>0.2</sub>O<sub>2</sub> Cells: Experimental Investigation and Application of the Multi-Site, Multi-Reaction Model. *Frontiers in Energy Research* **2022**, *10*, 671.
- (68) Baker, D. R.; Verbrugge, M. W.; Gu, W. Multi-species, multi-reaction model for porous intercalation electrodes: Part II. Model-experiment comparisons for linear-sweep voltammetry of spinel lithium manganese oxide electrodes. *Journal of The Electrochemical Society* **2019**, *166*, A521.
- (69) Shockley, W.; Read Jr, W. Statistics of the recombinations of holes and electrons. *Physical review* **1952**, *87*, 835.
- (70) Hall, R. N. Electron-hole recombination in germanium. *Physical review* **1952**, *87*, 387.
- (71) Bousse, L.; De Rooij, N. F.; Bergveld, P. The influence of counter-ion adsorption on the  $\psi_0$ /pH characteristics of insulator surfaces. *Surface science* **1983**, *135*, 479–496.
- (72) Protas, B.; Bewley, T. R.; Hagen, G. A Computational Framework for the Regularization of Adjoint Analysis in Multiscale PDE Systems. *J. Comput. Phys.* **2004**, *195*, 49–89.

- (73) Mistry, A.; Verma, A.; Sripad, S.; Ciez, R.; Sulzer, V.; Brosa Planella, F.; Timms, R.; Zhang, Y.; Kurchin, R.; Dechent, P. et al. A Minimal Information Set To Enable Verifiable Theoretical Battery Research. *ACS Energy Letters* **2021**, *6*, 3831–3835.